Acta Materialia 158 (2018) 214–229

Contents lists available at ScienceDirect

Acta Materialia

journal homepage: www.elsevier.com/locate/actamat

Full length article

Rational design of a lean magnesium-based alloy with high age-hardening response

M. Cihova [a, *], R. Schäublin [a, b], L.B. Hauser [a], S.S.A. Gerstl [a, b], C. Simson [c], P.J. Uggowitzer [a], J.F. Löffler [a, **]

[a] Laboratory of Metal Physics and Technology, Department of Materials, ETH Zurich, 8093 Zurich, Switzerland
[b] Scientific Center for Optical and Electron Microscopy, ETH Zurich, 8093 Zurich, Switzerland
[c] AIT Austrian Institute of Technology GmbH, Light Metals Technologies, LKR, 5282 Ranshofen, Austria

ARTICLE INFO

Article history:
Received 23 May 2018
Received in revised form
18 July 2018
Accepted 22 July 2018
Available online 24 July 2018

Keywords:
Mg–Al–Ca–Mn alloy
Age hardening
Microstructure
Transmission electron microscopy
Atom probe tomography

ABSTRACT

Magnesium-based alloys that allow fast processing, easy formability and subsequent age hardening to their final strength are highly desirable for lightweight structural applications. In this study, a lean age-hardenable wrought Mg–Al–Ca–Mn alloy, which combines precipitation hardening and grain refinement by secondary-phase pinning, was designed via thermodynamic calculation. The resulting alloy, AXM100, with a nominal composition Mg-Al0.6-Ca0.28-Mn0.25 (in wt.%), shows a remarkable improvement in tensile yield strength of 70 and 100 MPa upon artificial aging from the *as-extruded* state (*T5*) and the *solution-heat-treated* state (*T6*), respectively, reaching 253 MPa for the latter. A multi-scale microstructural analysis, combining light microscopy, transmission electron microscopy and atom probe tomography, was performed. It revealed a fine dispersion of Al–Mn precipitates with a β-Mn structure and Al–Ca-rich *Guinier–Preston* (G.P.) zones, which have an Al-to-Ca ratio of about 2. The former are responsible for impeding grain growth and the latter for age hardening. In addition, a fine dispersion of nanometric Ca-rich clusters preceding the G.P.-zone formation were identified which may contribute to strength. While the microstructural analysis, in terms of volume fraction and composition of the phases, reveals the limitation of the calculations, the latter successfully predict the elements contained in the various phases that play a key role in the mechanical properties, thereby proving them to be an invaluable tool for alloy design. In fact, the alloy designed in this study shows, despite its leanness, an age-hardening potential of 87 MPa and 118 MPa per 1 at.% total alloying content for the *T5* and *T6* condition, respectively, which is the highest among the compositions known for this type of alloys.

1. Introduction

Simultaneous high formability and high strength are required for magnesium (Mg) alloys if they are to be more widely deployed as lightweight structural materials in automotive, high-speed rail or aircraft applications, and to be competitive to their aluminum counterparts. Reducing the alloying content can significantly improve their formability [1,2] and thereby render their processability, e.g. by extrusion or rolling, economically more attractive. However, a lean-design concept appears counter-intuitive in terms of the desired high strength. Indeed, while an alloy's strength is generally governed by the combined contribution of solid-solution strengthening, precipitation hardening and grain-boundary strengthening, the former two become limited in case of a reduced alloying content. In terms of grain-boundary strengthening, the *Hall–Petch* relationship is mentioned, which describes the dependence of tensile yield strength (*TYS*) on grain size [3,4]. The *Hall–Petch* constant amounts for Mg to 150–250 MPa $\mu m^{1/2}$ [5,6], which is significantly larger than the one for polycrystalline aluminum (Al) at about 40 MPa $\mu m^{1/2}$ [7], showing the significance

* Corresponding author.
** Corresponding author.
E-mail addresses: martina.cihova@mat.ethz.ch (M. Cihova), joerg.loeffler@mat.ethz.ch (J.F. Löffler).

https://doi.org/10.1016/j.actamat.2018.07.054
1359-6454/

of grain refinement for Mg and its alloys. Strategies for achieving the fine-grained microstructure desired include severe plastic deformation (SPD), such as multi-pass equal-channel angular pressing [8] or high-pressure torsion [9], and powder metallurgical routes [10], but are limited by a low processing rate and cannot be easily scaled up.

Wrought alloys are attractive in terms of a high processing output. However, the high processing temperatures required significantly coarsen the grains and, thus, reduce the final strength [11,12]. This may be compensated by dispersing secondary-phase particles that can pin grain boundaries, thereby suppressing grain growth [13]. Their presence, however, can result in an increased extrusion force required to shape the material. Lean age-hardenable wrought Mg-alloys have thus received considerable attention because of their potential to achieve the desired combination of easy formability with high strength of the final part; the latter obtained by means of precipitation hardening in an artificial-aging treatment following hot forming. A variety of Mg-based alloying systems are suitable for precipitation hardening [14]. Their effectiveness for age hardening is, however, often impaired by the overly coarse nature of precipitates [15,16]. Indeed, dislocation motion is most effectively restricted by a high number of fine and uniformly dispersed precipitates [13]. Moreover, as in Mg-alloys it is the basal slip that dominates, precipitates located on the basal plane should most effectively increase the alloy's strength. This can be achieved by the precipitation of a metastable, fully coherent phase condensating as mono-layered, nanometric plates on its basal plane in large numbers, referred to as *Guinier–Preston* (G.P.) zones [14]. Many alloys containing rare-earth elements (REE) such as Y, Gd or Nd would satisfy this condition [14]. However, in light of the growing environmental and economic awareness, new alloys are to be designed that get by without their use.

In this study we focus on the Mg–Al–Ca–Mn system, referred to as AXM, because it appears to fulfill the requirements of easy formability, high age-hardenability and low-cost REE-free composition [17–20]. Pioneering work on this system was done by Nakata et al. [17], who demonstrated a remarkable age-hardening potential for this system. In our study, we challenge the AXM system with the aim of optimizing its age-hardening potential while minimizing its alloying-element content.

2. Design concept

In the following, we present our design concept which builds on the simultaneous contribution of grain-boundary strengthening and precipitation hardening. This requires thermally stable precipitates for grain refinement and a post-extrusion artificial-aging treatment for a fine dispersion of G.P. zones. We performed thermodynamic calculations to identify a suitable alloy design which comprises both the alloy composition and the thermomechanical processing route (Fig. 1).

As a boundary condition for the calculations, the maximum total alloying content was set at 1 at.%. This lean-alloy concept, firstly, allows a *solution-heat-treatment (sht)* window for the relevant elements constituting the hardening phase, bringing them into solid solution for an effective hardening potential instead of the otherwise occurring coarse precipitation [15,16]. Secondly, the leanness avoids a high solute content and a high volume fraction of

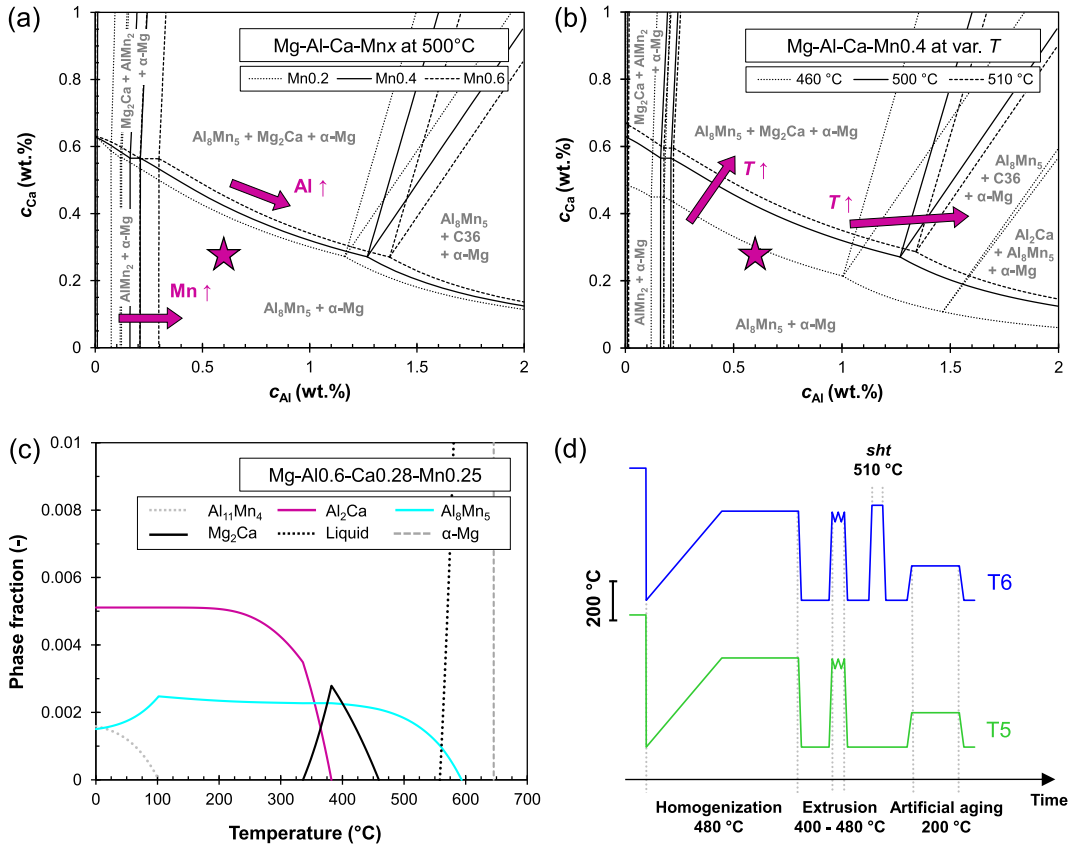

Fig. 1. Calculated phase diagrams of AXM as a function of Al and Ca with variations of (a) Mn content and (b) temperature. (c) Phase fraction as a function of temperature for the resulting alloy Mg-Al0.6(0.54)-Ca0.28(0.17)-Mn0.25(0.11) in wt.% (in at.%) (AXM100). (d) Thermomechanical processing sequence defining the *T5* and *T6* tempers. The composition of the optimized alloy is marked with a star in (a) and (b).

secondary phases, thus minimizing the force required for hot forming [21]. In the following, we present first the design rules for bringing an effective precipitation hardening by G.P.-zone formation, and then the strategy for achieving grain refinement.

2.1. Hardening phase: G.P. zones as precursors of the Al_2Ca phase

Both binary alloys Mg–Ca and Mg–Al show only a limited aging potential [14,22,23], but the simultaneous addition of Al and Ca to Mg can significantly increase the hardening response [22,24]. Jayaraj et al. [22] demonstrated that the trace addition of 0.3 wt.% Al to binary Mg-Ca0.5 (wt.%) enhances the hardness increment significantly, from $\Delta H_V = 10$ without Al to $\Delta H_V = 32$ with Al. This was attributed to the formation of G.P. zones that form at low temperature upon disintegration of a super-saturated solid solution (*SSSS*). They are believed to have a C15 structure and to be the precursors of the fcc/C36 Al_2Ca equilibrium phase [19,22,24]. These G.P. zones constitute the hardening phase considered in our alloying design. Because their precipitation is reported to originate from *SSSS* [14], the alloy composition is to be balanced accordingly to allow for an *sht* window which provides sufficient amounts of Ca and Al in solid solution to form those G.P. zones upon artificial aging. As the precise composition and structure of the G.P. zones are still unknown, the present alloy design relies on thermodynamic calculations which predict the Al_2Ca phase, i.e. assume an Al-to-Ca atomic ratio of 2.

The alloy's total amount of Al and Ca, as well as their ratio, appear to sensitively govern the level of the aging response [18,22]. The lower concentration limit of both elements is set by their solubility in Mg, which restricts their driving force to precipitate. This is more pronounced for Al, which has a significantly higher solubility in Mg than Ca. The upper concentration limit, in contrast, is mainly defined by Ca: on the one hand, ease of formability is known to decline severely with increased Ca content [20,21]; on the other hand, the low solubility of Ca in Mg [25] stabilizes the Mg_2Ca phase even at low Ca amounts (Fig. 1a). The solubility of Ca and the Mg_2Ca phase is further decreased by the presence of Al (Fig. 1a). An excess of the Al and Ca content is reached when it impedes the possibility of the *sht* window required to obtain an *SSSS* for Ca. This would promote the coarse formation of equilibrium phases Mg_2Ca (C14), Al_2Ca (C15), $(Mg,Al)_2Ca$ or $(Al,Mg)_2Ca$ (both C36). This is detrimental in two ways: first, the amount of Al and Ca in solid solution is depleted, which in turn impedes the formation of the desired G.P. zones; second, the coarse precipitation of equilibrium phases is impairing the mechanical performance because they may act as crack-initiation sites [18]. With regard to their ratio, the assumed composition for the desired G.P. zones of Al_2Ca is recalled, which suggests that the minimum required concentration of Al should amount to twice that of Ca. The sensitivity with which the Al-to-Ca ratio determines the hardening potential is evident from the aforementioned work by Jarayaj et al. [22], who studied the aging potential of dilute Mg–Al–Ca alloys with varying Al-to-Ca ratios by adjusting the Al content at a constant Ca content of 0.5 wt.%. In fact, they observed an enhanced hardness increment with the successive increase in the Al content from 0 to 0.1 to 0.3 wt.% Al. However, the expected increase with further Al addition could not be achieved. This is probably due to surpassing the upper limit for Al and Ca, thereby promoting the formation of coarse Mg_2Ca phase (Fig. 1a) and thus limiting the hardness potential.

2.2. Grain refinement via thermally stable Al_8Mn_5 dispersoids

Before considering the simultaneous presence of Al, Ca and Mn in Mg, we will examine the isolated impact of Mn in Mg. Mn addition was shown to refine the grain size in several wrought Mg alloys [26–29]. In Al-containing wrought Mg alloys, this grain refinement is explained by the formation of Al–Mn dispersoids that retard grain growth by pinning the grain boundaries [20,28]. Due to their high thermal stability, with a predicted solvus temperature at 600 °C for the optimized alloy composition of this study (Fig. 1c), this effect should persist at elevated processing temperatures. According to *Zener* [13], the pressure with which grain-boundary motion is restricted by such secondary-phase precipitates increases with a reduction of their size, given a constant volume fraction. The processing-related measures taken to obtain the characteristics required of such dispersoids are presented below in the section on *thermomechanical conditions*.

Finally, when concurrently adding Al, Mn and Ca to combine the effects of grain-boundary pinning by thermally stable Al–Mn dispersoids and age hardening via G.P. zones with an assumed Al_2Ca composition, the consumption of Al by Mn for the formation Al–Mn phase needs to be taken into account. Note that the Al–Mn phase is stable in the *sht* temperature regime (Fig. 1c). With this in mind, only the remaining Al content in solid solution that was not consumed by Mn is available to form the hardening Al–Ca phase during artificial aging. Assuming the Al–Mn phase to be of the type Al_8Mn_5, as reported in literature [30] and predicted by the calculations (Fig. 1) [31], an excess of Al over Mn is essential. The required extent of Al excess is, in turn, set by the Ca content available in solid solution at the *sht* temperature chosen, and should correspond to the Al-to-Ca atomic ratio of 2. This set of rules is confirmed by a study conducted on Mg-Al0.27-Ca0.13-Mn0.21 (in at.%) with a corresponding Al-to-Mn atomic ratio of about 5 to 4 [32]. Besides a generally satisfying mechanical performance, this alloy showed only a marginal age-hardening response of about $\Delta H_V = 7$, corresponding to an increase of roughly 16% [32]. Another study, conducted on Mg-Al0.3-Ca0.2Mn*x* (in at.%), showed that an increase in Mn content from 0.1 to 0.2 at.% caused the alloy's aging response to deteriorate significantly [33]. On this basis, maximizing the Ca content in solid solution with subsequent appropriate balancing of Al and Mn appears reasonable. The Ca content, however, needs to be kept within the limits to still allow the required *sht* window for Ca. Fig. 1b shows, using the example of a constant Mn content of 0.4 wt.%, that Ca can be fully solubilized at temperatures above 460 °C. While the solubility can be increased further with temperature (Fig. 1b), it is limited by the solidus temperature, which is predicted to be 517 °C for the optimized composition (Fig. 1c). It is also evident that a high Ca content in solid solution can only be obtained when both Ca and Al are kept low (Fig. 1b), thereby underlining the essence of the lean-alloying design.

2.3. Thermomechanical conditions

Fig. 1d depicts the sequence of thermomechanical conditions applied to explore the potential of the alloy design presented. It comprises fast cooling from the melt to avoid precipitation during cooling, followed by a homogenization heat treatment. The latter features slow heating to an intermediate temperature: this is envisioned to generate the desired fine precipitation of the Al–Mn dispersoids in a high number density. Their formation before extrusion is crucial if they are to act as obstacles to grain-boundary motion during dynamic recrystallization and during heat treatments after extrusion. A high extrusion temperature of 400–480 °C was chosen with the aim of achieving easy formability, and to bring a high fraction of Ca into solid solution in the *as-extruded* state (Fig. 1b and c). In fact, an extrusion temperature exceeding the solvus temperature of the Mg_2Ca phase is desired because the resulting high solute content in the *as-extruded* condition may render a subsequent *sht* unnecessary, i.e. a *T5* condition would correspond to a pseudo-*T6* condition, and would therewith result in

economically more attractive processing routes. This temperature is predicted to be 460 °C. In a final step, an artificial-aging treatment was performed in the temperature range of 175 and 225 °C, which seems to be a compromise between sufficiently fast aging and a low risk for rapid overaging.

Taking these design aspects into account, a lean AXM alloy was designed with composition Mg-Al0.6(0.54)-Ca0.28(0.17)-Mn0.25(0.11) in wt.% (in at.%). The corresponding phase diagram is presented in Fig. 1c. In the following, we validate the design concept by thoroughly investigating the microstructure-mechanical properties relationships by means of multiscale microstructural investigations using light microscopy, transmission electron microscopy and atom probe tomography. The microstructural insights gained are used to assess the validity of the predicted phases via thermodynamic calculation.

3. Materials and methods

3.1. Thermodynamic calculations

Thermodynamic calculations of possible phases in AXM were performed using the Pandat™ software package for multi-component systems, taking input from the PanMg2018_TH [31] database. All the calculations presented in this study assume thermodynamic equilibrium.

3.2. Processing

The alloy with nominal composition Mg-Al0.6(0.54)-Ca0.28(0.17)-Mn0.25(0.11) in wt.% (in at.%), hereafter referred to as AXM100, was prepared by melting of Mg (99.95% purity), Al (99.7%), Ca (98.5%) and Mn (as $MnCl_2$ compound, 98.5%) in a graphite crucible in a resistance oven under an Ar/SF_6 atmosphere at 700 °C. The crucible was cooled quickly to room temperature on a water-cooled cupper block to avoid precipitation during cooling. The ingots were homogenized by heating to 480 °C at a rate of 4 K min^{-1} and kept at that temperature for 6 h in order to form the Al–Mn dispersoids. Ingots were extruded into bars of 10 mm diameter using a direct extrusion process at 400, 450 and 480 °C with a ram speed of 0.5 mm s^{-1} to 2.5 mm s^{-1} and an extrusion ratio of 25, corresponding to exit speeds of 750 to 3750 mm min^{-1}, respectively. Cooling with pressurized air was applied on the bars close to the exit position of the extrusion machine. Both alloy production and the extrusion process took place at *Leichtmetallkompetenzzentrum Ranshofen GmbH,* Austria. Note that the extrusion machine employed in this study has an upper force limit of 1.5 MN, requiring a minimum temperature of 400 °C to achieve the desired extrusion rates.

3.3. Artificial aging

In order to study the hardening potential of AXM100, artificial-aging treatments were performed for two thermomechanical conditions: *T5* temper, i.e. *as extruded* + artificially aged, and *T6* temper, i.e. solution-heat-treated (*sht*) + artificially aged (Fig. 1d) [34]. The artificial-aging treatment was performed in an oil bath at 200 °C for various durations ranging from 10 min to 72 h, followed by a water quench. The *sht* parameters of 510 °C and 10 min were chosen according to the predicted solvus temperature of the Mg_2Ca phase of 460 °C (Fig. 1c) and the alloy's liquidus temperature of 518 °C experimentally obtained using differential scanning calorimetry (data not shown). Note that this *sht* condition, which is a central part of our strategy, corresponds to a state in which Al_2Ca and Mg_2Ca phases should be completely dissolved, while the Al–Mn-rich phase is expected to persist (see Fig. 1). This *pseudo-sht* state, while admittedly not strictly complying with a solution-heat treatment, is intentional because the presence of such thermally stable Al–Mn dispersoids are meant to prevent grain growth at elevated temperatures.

The age-hardening response of AXM100 upon isothermal holding at 200 °C for the *T5* and *T6* condition was characterized by Vickers hardness under a load of 5 kg. Vickers hardness on the cross-sectional plane of the extrusion direction was determined at each time point with 10 averaged individual indents.

For a detailed analysis of the material's mechanical behavior and corresponding microstructure, four thermomechanical-treatment conditions were considered: (1) *as extruded*, (2) *peak-aged T5*, (3) *sht*, and (4) *peak-aged T6*. The *peak-aged* conditions present the duration of the artificial-aging treatments for which maximum hardness was obtained.

3.4. Tensile tests

Tensile specimens, with two specimens per condition, were prepared according to DIN 50125 (M5, diameter = 3 mm). All specimens were prepared from extruded bars parallel to the extrusion direction. Tests were conducted using a Schenck Trebel electromechanical universal testing machine with a 100 kN hydraulic load cell at room temperature and at a strain rate of 10^{-3} s^{-1}.

3.5. Microstructural analysis

3.5.1. Light microscopy

For grain-size analysis, samples of each condition were prepared by mechanical grinding and polishing followed by etching with picric acid to reveal the grain boundaries. Three individual micrographs per condition were analyzed by applying the linear intercept method (Lince®, TU Darmstadt).

3.5.2. Electron microscopy

Transmission electron microscopy (TEM) was performed to determine the chemical distribution of the alloying elements and the number density, size and spatial distribution of the precipitates present at the four different conditions. TEM specimens were prepared as standard 3 mm diameter disks by mechanically grinding the material to about 100 μm thickness and punching it into a 3 mm disk, followed by Ar-ion milling to achieve electron transparency using a precision ion polishing system (PIPS™ II) from GATAN®. Ion milling was performed at liquid nitrogen temperature to prevent changes in the microstructure.

TEM imaging was performed in an FEI Talos™ F200X operated at 200 kV and equipped with a field-emission gun. Imaging was mainly performed in scanning TEM mode with a high-angle annular dark-field detector (HAADF-STEM mode) at a camera length of 98 mm to reveal the secondary phases. In HAADF-STEM imaging mode, the resulting image gives a contrast that is proportional to about $Z^{3/2}$, with Z being the atomic number. To reveal the G.P. zones, the camera length was adjusted to 145 mm. At least three different areas per thermomechanical condition were assessed to determine the precipitate's number density and size. The number density *N* was evaluated by manual counting of the precipitates in a given area and their size was determined by manually measuring the diameter in ImageJ software. The relative error on *N* is associated to the statistical error $\frac{1}{\sqrt{n}}$ with *n* being the number of precipitates counted in the micrographs. In this study *n* was between 400 and 1600, resulting in a relative error on *N* between 2.5 and 5%. The TEM-foil thickness, necessary to estimate the number density of precipitates and G.P. zones, was determined using stereographic pairs of images taken at +15° and −15°.

Elemental distribution maps were recorded by energy

dispersive X-ray spectroscopy (EDS) performed with an FEI Super-X detector. The acquisition time for each map was 15 min, providing a good compromise between adequate noise reduction in the data and minimization of beam damage, with a dwell time of 10 μsec to further minimize beam damage during mapping.

Electron diffraction patterns were obtained for the Al–Mn-rich precipitates in nanodiffraction mode at 80 kV to avoid beam damage. Spot patterns were acquired for two zone axes and analyzed using CrysTBox diffractGUI software [35], and were compared with simulated patterns obtained using jEMS software [36].

3.5.3. Atom probe tomography

Specimens from the *peak-aged T6* condition were prepared for atom probe tomography (APT) by mechanically tripod-polishing a wedge-shaped 3 mm disk, followed by Ar-ion milling in a PIPS™-II (Gatan®) and finally shaping it into APT tips using an FEI Helios 600i dual-beam focused ion beam (FIB-SEM) instrument. Annular milling of the tips resulted in APT tip apex radii of about 50 nm. The tips were vacuum-transferred from the FIB directly into the Cameca local electrode atom probe (LEAP™ 4000X-HR™) tomograph to avoid oxidation, with a vacuum environment remaining below 10^{-5} mbar at all times. The acquisition was performed at 65 K in laser-pulsed mode, applying a 200 kHz frequency of 150 pJ energy, resulting in an Mg^{++}/Mg^{+} Charge-State-Ratio (CSR) of 0.3. 3D-reconstruction and analysis were performed using IVAS 3.6.14 software from Cameca. The default reconstruction parameters were deemed satisfactory after correlating the resulting reconstruction with the observed nanostructures in TEM.

4. Experimental results

In the following sections, we first present the impact of processing conditions on the quality of the extruded AXM100 material before focusing on the aging response of AXM100. We then take the conditions that lead to the greatest hardening, referred to as the *peak-aged* condition, to elucidate the mechanical properties and their microstructure; with the aim of establishing a detailed understanding of the microstructure-property relationships in AXM100.

4.1. Processability

Fig. 2 depicts the processing outcome at varying extrusion exit speeds and temperatures, evaluated by visual inspection of the resulting surface quality. It was rated as defect-free, as containing micro-cracks, or as containing severe surface cracks (Fig. 2b). The latter occurred when either a too high extrusion temperature, a too high speed, or a combination of both were deployed (Fig. 2b, red crosses). This characteristic repetitive circumferential cracking, referred to as *fir-tree cracking* or *speed cracking*, is a common phenomenon occurring in hot extrusion, and is attributed to local melting caused by friction-induced heating during the deformation process [37]. At lower temperatures or lower speeds the resulting surface quality is adequate. The processing window identified for the applied 'direct extrusion' is marked by a green triangle in Fig. 2. Note that extrusion was limited to a minimum extrusion temperature of 400 °C by the extrusion force of the system used.

To select the best extrusion condition in this processing window, the hardening potential following extrusion was additionally considered. From an economic point of view, a *T5* treatment is preferable to a *T6* treatment, because it requires no additional *sht*. A sufficient age-hardening response under such conditions requires sufficient availability of dissolved Ca and Al in the extruded material for the desired formation of the hardening Al_2Ca phase upon artificial aging. For Ca, this requirement implies the need to dissolve the Mg_2Ca phase, which would otherwise consume most of the Ca. To satisfy this condition, the extrusion temperature chosen must be above or close to the solvus temperature of the Mg_2Ca phase, which, according to the phase diagram in Fig. 1c, is 460 °C. For Al, sufficient amounts in solution for the formation of the Al_2Ca phase is ensured for the full temperature range from room temperature to above the melting temperature, according to the design concept of this study. This takes the consumption of Al by Mn to form Al_8Mn_5 into account, yet leaves a sufficient quantity dissolved in the Mg matrix for the formation of the Al_2Ca hardening phase.

With this in mind, and considering the processing window, indicated by the green triangle in Fig. 2, rods extruded at the

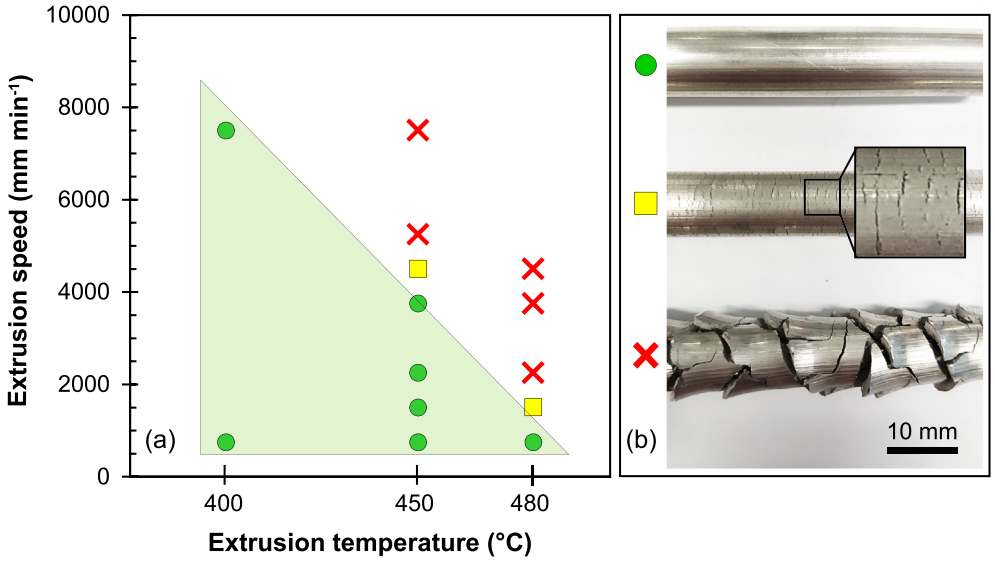

Fig. 2. (a) Qualitative assessment of the extrusion outcome for various extrusion speeds and temperatures as evaluated by the surface quality. Each data point represents an individual extrusion process. The surface quality was rated as either defect-free (green circles), as containing micro-cracks (yellow squares) or as containing severe surface cracks (red crosses). (b) Representative photographs of these three conditions. Only extruded bars with defect-free surfaces were selected for this study. (For interpretation of the references to color in this figure legend, the reader is referred to the Web version of this article.)

intermediate temperature of 450 °C were chosen for the detailed analysis of AXM100. This ensures a good surface quality and potentially good hardening capability upon artificial aging.

4.2. Hardening response

The following section presents the hardening response of AXM100 upon isothermal aging at 200 °C, comparing two initial conditions, the *as-extruded* (*T5* temper) and *sht* condition (*T6* temper), and two different extrusion exit speeds.

Fig. 3 shows the Vickers hardness as a function of artificial-aging time at 200 °C and at two extrusion speeds (slow at 750 and fast at 3750 mm min^{-1}) for AXM100 in *T5* and *T6* temper. Considering first the slow extrusion speed, the material in its *as-extruded* condition exhibits an average $H_V = 47.3 \pm 0.6$. Upon isothermal aging at 200 °C, the hardness increases steadily with $\Delta H_V = 3.8$ to $H_V = 51.09 \pm 1.2$ within the first 60 min; from this point onwards the hardening rate slows down significantly, increasing only marginally with prolonged aging time and reaching its maximum of $H_V = 54.03 \pm 1.0$ after 48 h. In the *sht* condition the hardness is slightly reduced to $H_V = 44.5 \pm 1.6$. However, upon isothermal holding at 200 °C it increases rapidly and reaches a peak hardness after only 2 h with an increase of $\Delta H_V = 17$ to $H_V = 61.8 \pm 1.2$, followed by a slight decrease for prolonged aging times, to H_V of 58.4 ± 1.7 at 72 h.

With respect to the processing speed, it appears that for *T5* condition the hardness potential is greater when the extrusion is faster (Fig. 3), amounting to an enhancement from $\Delta H_V = 3.8$ when extruded slowly to $\Delta H_V = 5.3$ after 60 min, and to $\Delta H_V = 6.3$ after 2 h, when extruded faster. In contrast, the hardening response of the *T6* condition seems to be independent of the processing speed, reaching $\Delta H_V = 17.3$ and $\Delta H_V = 16.7$ for slow and fast extrusion, respectively, both achieved after 2 h. Nevertheless, the overall hardening response of the *T5* condition upon aging stays always considerably below that of the *T6* condition, regardless of the extrusion speed.

For all further analyses, the aging time to achieve peak aging was set to 90 min for both *T5* and *T6*. This duration represents a compromise between the time required to achieve peak-hardness for *T5*, i.e. 1 h, and *T6*, i.e. 2 h. Furthermore, the material extruded at 750 mm min^{-1} was chosen for the detailed analysis due to the material's lower risk at slower processing rates to show impairment by microstructural changes, induced by speed cracking, which may visually be non-detectable.

4.3. Tensile behavior

Fig. 4 presents the engineering stress–strain response in tension for AXM100 in its *as-extruded* and *sht* condition, plus in the corresponding *peak-aged T5* and *T6* conditions, respectively.

For the *peak-aged T5* temper, a significant increase in the tensile yield strength (*TYS*) of about 70 MPa relative to the *as-extruded* condition was observed, corresponding to an increase of ~43%, reaching 236 MPa. This contrasts with the small increment of the hardening response of 8.5%, evaluated by Vickers hardness, corresponding to $\Delta H_V = 4$. Note that this increase was achieved after only 90 min of artificial aging at 200 °C. For the *peak-aged T6* temper, a remarkable increase in the *TYS* of close to 100 MPa relative to the *sht* condition was achieved, corresponding to an increase of ~62%, reaching 253 MPa (Fig. 4).

A satisfying elongation to fracture (A_f) of 14% is observed for the *as-extruded* condition. The material suffers, however, from a drastic reduction thereof in the different heat-treated conditions, with an average of 9% in the *sht* condition and 7 and 8% in the *peak-aged T5* and *peak-aged T6* condition, respectively. The shapes of the stress–strain curves presented in Fig. 4 indicate that specimens in the heat-treated conditions suffer from premature failure which occurred before the ultimate tensile strength (*UTS*) was reached.

Table 1 summarizes the values of *TYS*, *UTS* and A_f determined in the tensile tests.

To understand the microstructural relationships to the mechanical properties, a detailed microstructure analysis of samples of all four thermomechanical conditions, i.e. *as extruded*, *sht*, *peak-aged T5* and *peak-aged T6*, was performed.

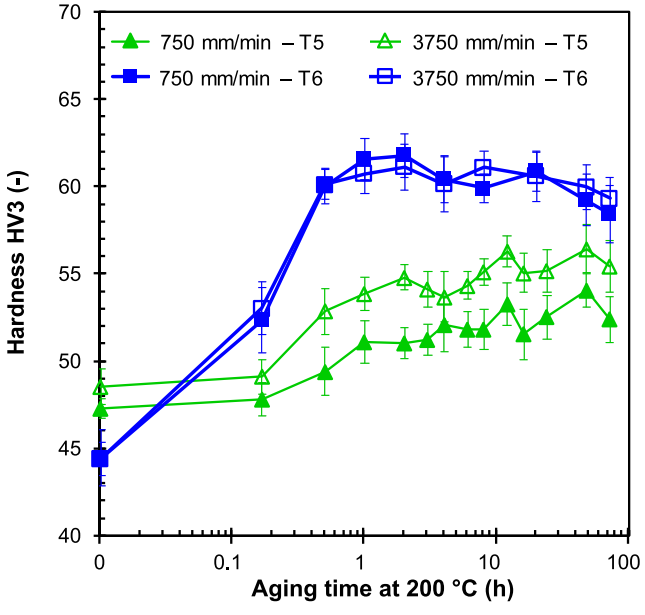

Fig. 3. Vickers hardness of AXM100 as a function of artificial aging time at 200 °C starting from the *as-extruded* state (*T5* temper) and from the *sht* state (*T6* temper) and processed at two different extrusion exit-speeds, 750 and 3750 mm min^{-1}.

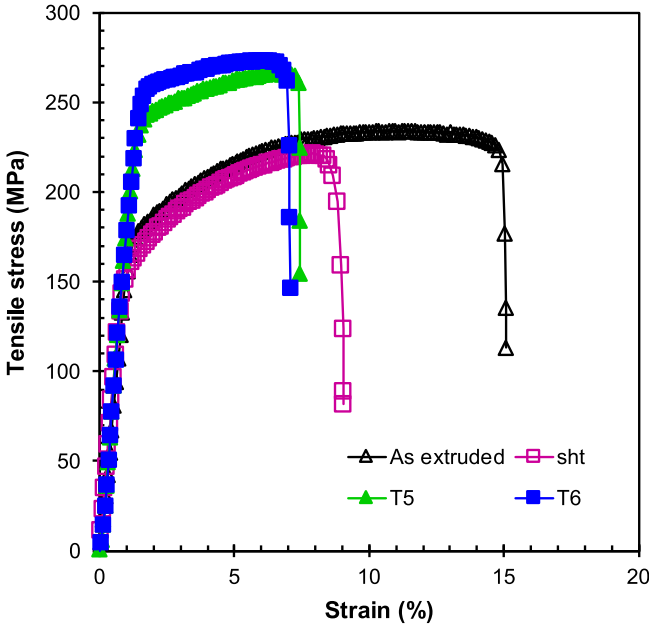

Fig. 4. Stress–strain response to tensile-loading condition of AXM100 for the four different thermomechanical treatment conditions.

Table 1
Mechanical properties of AXM100 evaluated upon tensile testing at room temperature. *TYS*: tensile yield strength; *UTS*: ultimate tensile strength; A_f: elongation to fracture.

Condition	*TYS* (MPa)	*UTS* (MPa)	A_f (%)
As extruded	165 ± 7.8	232 ± 2.7	14 ± 0.3
Peak-aged T5	236 ± 2.1	265[a] ± 1.9	7 ± 1.1
sht	156 ± 0.1	225[a] ± 5.3	9 ± 2.5
Peak-aged T6	253 ± 0.2	277[a] ± 4.2	8 ± 2.9

[a] Failure before *UTS* was reached.

4.4. Microstructural investigations

4.4.1. Light microscopy

Fig. 5 depicts optical micrographs of the *as-extruded* and *sht* conditions along with the corresponding grain-size histograms. The optical micrograph of the *as-extruded* condition reveals an almost fully recrystallized microstructure with an average grain size of about 27 ± 18 μm (Fig. 5a). The corresponding grain-size histogram clearly shows a substantial proportion of considerably smaller grains below 12 μm (Fig. 5c). The optical micrograph of the *sht* condition shows that the high temperature during *sht* at 510 °C for 10 min induced on the one hand static recrystallization, resulting in a fully recrystallized microstructure, but on the other hand a slight grain growth, increasing the average grain size to 34 ± 18 μm (Fig. 5b). The ratio of small grains below 12 μm significantly declined upon *sht*, as visible from this micrograph (Fig. 5b) and supported by the corresponding grain-size histogram (Fig. 5d).

The low-temperature exposure during artificial-aging treatment at 200 °C for 90 min did not result in further grain growth and the average grain size was determined to be 29 ± 9 and 32 ± 12 μm for *peak-aged T5* and *T6*, respectively (not shown).

While the average grain size was approximately the same for all conditions, areas with significantly larger grains ($d > 60$ μm) are present, predominantly in the *sht* condition.

4.4.2. Electron microscopy

Fig. 6 presents representative STEM HAADF images at moderate magnification and the corresponding STEM EDS maps of the four thermomechanical conditions, revealing the characteristics of secondary-phase precipitates in terms of their spatial distribution, number density and size, as well as their chemical composition.

In the HAADF micrographs in Fig. 6a–d, the secondary-phase precipitates appear brighter than the Mg matrix, corresponding to the presence of elements heavier than Mg, thereby indicating Ca, Al and/or Mn in the precipitates. Those nanometer-scaled precipitates appear homogeneously distributed across the grains.

The corresponding EDS maps in Fig. 6a–d reveal that these finely distributed secondary-phase precipitates are of two types: either single-precipitated Al–Mn-rich dispersoids, or two adjacent precipitates with one being an Al–Mn-rich dispersoid and the other being an Mg–Ca-rich phase. Such two-sided precipitates are referred to as Janus particles to account for the co-presence of two phases (Fig. 7).

While the Al–Mn dispersoids are present in all four thermomechanical conditions and are homogeneously distributed across the grains, the Janus particles are only observed in the *as-extruded* (Fig. 6a) and *peak-aged T5* (Fig. 6c) condition. Note that matrix regions close to grain boundaries lack them. It appears that the number density of the Janus particles is reduced in the *peak-aged T5* condition compared to the *as-extruded* condition. Some of them are marked with white arrows in Fig. 6c. The characteristics of these two types of precipitates are described in detail further below. In addition, a third phase is present that is

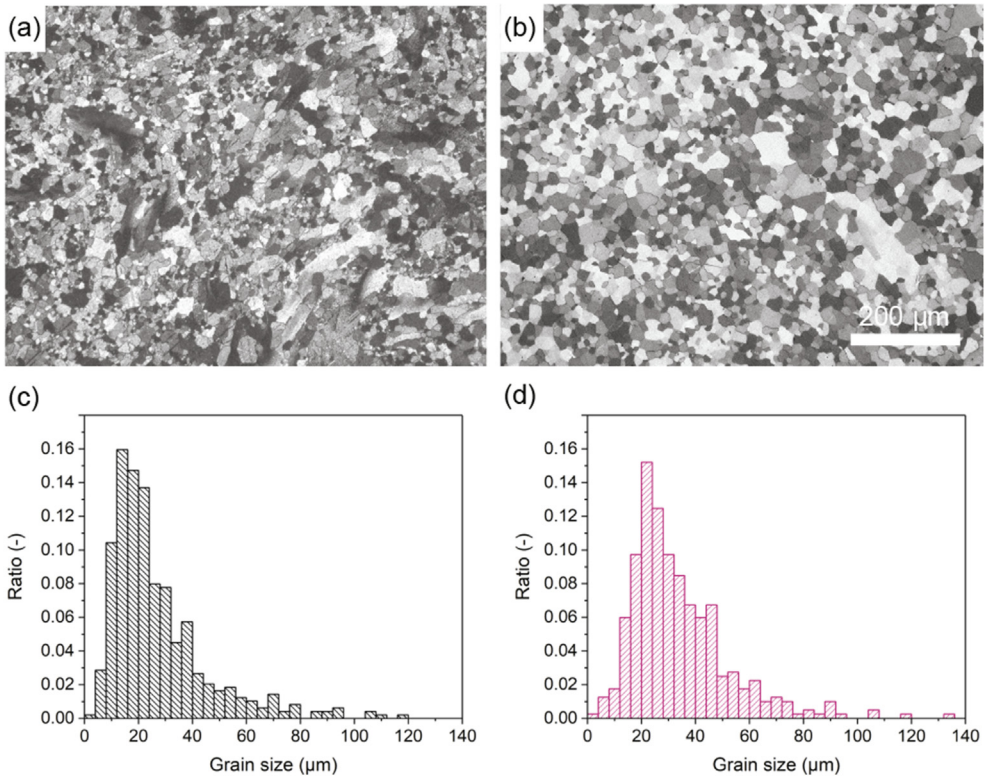

Fig. 5. Light micrographs and grain-size histograms derived for the (a + c) *as-extruded* and (b + d) *sht* conditions. The micrographs show cross-sections taken perpendicularly to the extrusion axis. The scale bar is indicated in (b).

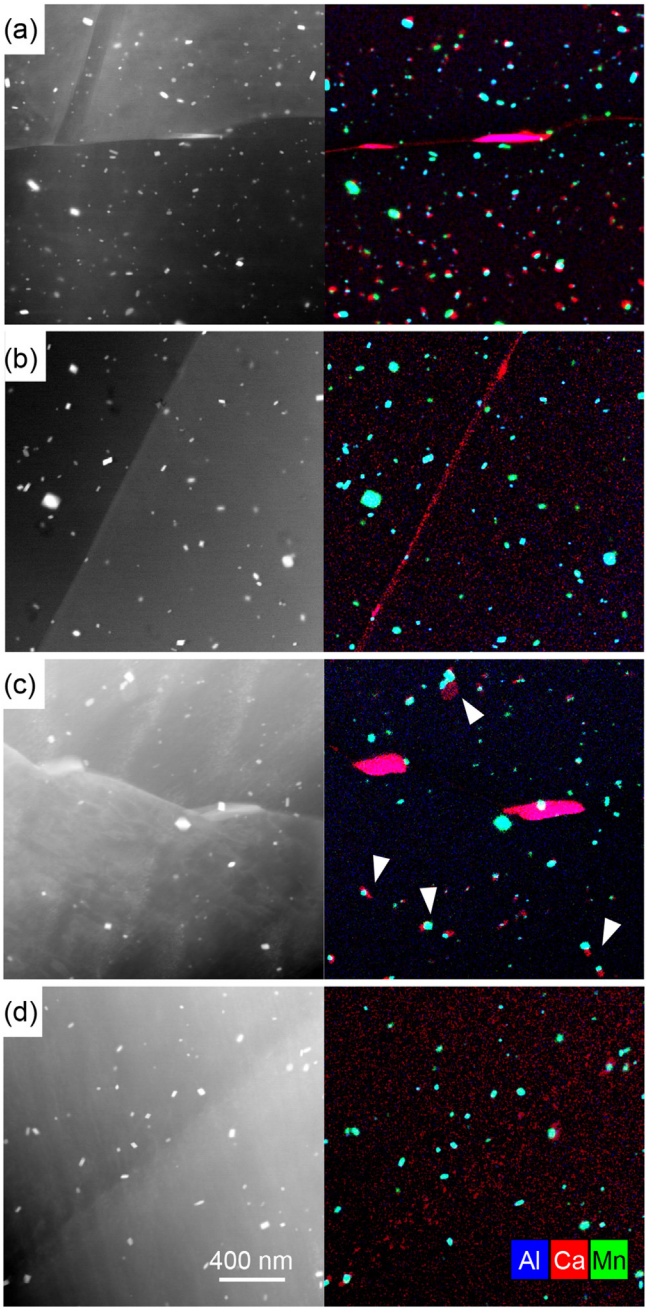

Fig. 6. STEM HAADF images and corresponding STEM EDS chemical maps of the four thermomechanical conditions: (a) *as extruded*; (b) *sht*; (c) *peak-aged T5*; and (d) *peak-aged T6*. The elemental color code for EDS maps and the scale bar are indicated in (d). (For interpretation of the references to color in this figure legend, the reader is referred to the Web version of this article.)

more scattered, coarser and usually in the form of elongated precipitates located at the grain boundaries (clearly visible in Fig. 6a and c, but also observed in the other conditions). EDS maps reveal that they consist of about 62 at.% Mg, 27 at.% Ca and 7 at.% Al. The elemental ratios suggest that they are of type $Mg_2(Ca,Al)$. Note that no grain-boundary bowing around such precipitates is observed, which would indicate a role as obstacles to grain-boundary motion.

Lastly, Ca segregation at the grain boundaries is evident for all conditions, which is accompanied by its depletion in their vicinity.

4.4.2.1. Al–Mn dispersoids. The number density of Al–Mn dispersoids was estimated from STEM stereo images and determined to be on the order of $5 \times 10^{19}\,m^{-3}$ for all conditions. Likewise, the dispersoids' size is comparable across the conditions and determined to be about 20 nm. Precise number densities and dispersoid sizes of the four conditions are given in Table 2.

The EDS spectrum displayed in Fig. 7d is typical of the Al–Mn dispersoids. It reveals that Mn is present in larger quantities than Al, with an Mn-to-Al ratio of about 2. Note that the EDS spectrum was acquired in very thin areas of the TEM foil, where the precipitate occupies the whole sample thickness and thus avoids the contribution of the matrix, increasing the accuracy of this analysis. The additional peaks at 0 keV and at 0.525 keV relate to the electronic noise of the EDS system and to oxygen contamination of the sample surface, respectively. APT analysis confirmed the higher Mn content compared to that of Al with a composition of the dispersoids determined as 57.6 at.% Mn, 40.4 at.% Al and 1.4 at.% Mg. This finding contradicts the thermodynamic simulation, which predicts an occurrence of the Al_8Mn_5 phase, and will be discussed later.

4.4.2.2. Janus particles. Fig. 7 depicts typical Janus particles, with the Mg–Ca phase co-precipitated at the site of the Al–Mn dispersoids. As mentioned above, they are referred to as Janus particles due to their co-appearance. Both sides are each about 10–30 nm in size. EDS analysis shows that Mg and Ca are present in a ratio of about 2 to 1 (Fig. 7c), which is typical of the Laves-type Mg_2Ca phase, as predicted by the thermodynamic calculation (Fig. 1c). The EDS spectrum further reveals some solubility of Al in Mg_2Ca.

The Janus particles appear in a high number density in the *as-extruded* state. Note, however, that in this condition, Al–Mn dispersoids are present without the simultaneous appearance of the Mg_2Ca phase in areas adjacent to the grain boundaries, where the matrix is generally depleted in Ca (Fig. 6a). In the *peak-aged T5* condition (Fig. 6c) Janus particles are also present, although in lower number densities than in the *as-extruded* condition. Upon exposure to 510 °C for 10 min, the Mg_2Ca phase dissolves and is thus observed neither in the *sht* (Fig. 6b) nor in the *peak-aged T6* condition (Fig. 6d).

4.4.3. High resolution electron microscopy

Fig. 8 presents high-resolution (HR)-STEM-HAADF images taken with the incident beam along the $<2\bar{1}\bar{1}0]$ (Fig. 8a) or $<10\bar{1}0]$ (Fig. 8b) zone axis of the Mg matrix. They reveal a dense dispersion of G.P. zones for *peak-aged T5* and *peak-aged T6* specimens. No G.P. zones were observed in the *as-extruded* and the *sht* condition. The G.P. zones are located on the basal plane of the Mg matrix, as revealed by the diffraction pattern in Fig. 8a. Note that the spot pattern corresponds to the Mg matrix only and does not reveal possible additional spots due to the presence of the G.P. zones. The inset to Fig. 8b shows a single, mono-layered G.P. zone.

The number density of G.P. zones was determined as $0.57 \times 10^{23}\,m^{-3}$ and $2.63 \times 10^{23}\,m^{-3}$ for *peak-aged T5* and *peak-aged T6*, respectively. No depletion of G.P. zones around the Al–Mn-rich dispersoids was observed for either temper. Their size was determined as 3.6 ± 0.8 nm and 2.8 ± 0.7 nm for the *peak-aged T5* and *peak-aged T6* condition, respectively. The number densities and sizes are given in Table 2.

4.4.4. Atom probe tomography

Fig. 9a depicts the atom map obtained by APT from the *peak-aged T6* temper. The sample volume of roughly 120 nm × 80 nm × 25 nm (viewed in the x-z projection) presents the matrix region between the Al–Mn dispersoids with a high number of G.P. zones. The sample comprises the edge of an Al–Mn dispersoid emphasizing its relative size difference with respect to the G.P. zones. In this

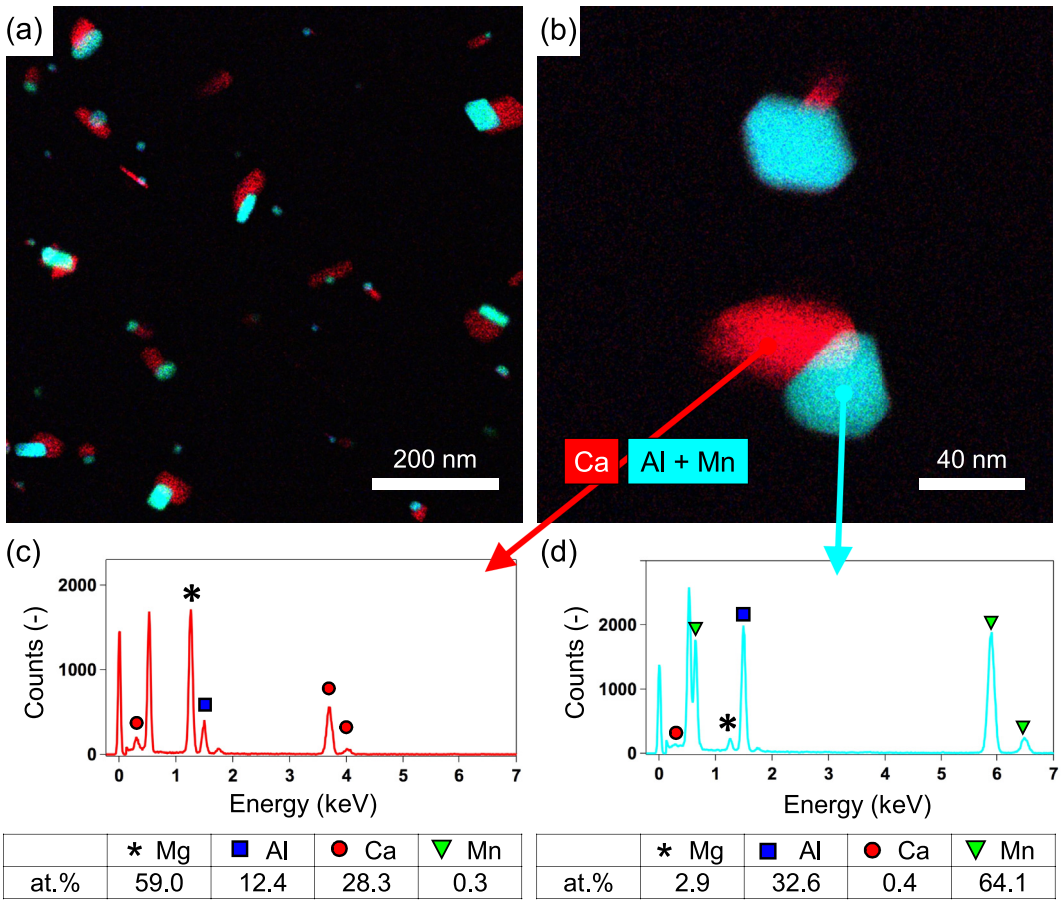

Fig. 7. Chemical map of the Janus particles. (a, b) STEM EDS chemical maps of the two phases composing a Janus particle. Quantified EDS spectra of (c) an Mg–Ca-rich precipitate and (d) an Al–Mn-rich precipitate. (For interpretation of the references to color in this figure legend, the reader is referred to the Web version of this article.)

Table 2
Number density N, diameter d and volume fraction f of Al–Mn dispersoids and *Guinier–Preston* zones for the four thermomechanical conditions considered. Spherical geometry was assumed for the Al–Mn dispersoids and plate geometry for the G.P. zones. The G.P.-zone volume was calculated with $d_{G.P.}$ as the plate diameter and the interplanar distance of the Mg crystal at about 0.26 nm as the plate thickness.

Condition	Al–Mn dispersoids			Guinier–Preston zones		
	N_{Al-Mn} (% Error) (m^{-3})	d_{Al-Mn} (nm)	f_{Al-Mn} (–)	$N_{G.P.}$ (% Error) (m^{-3})	$d_{G.P.}$ (nm)	$f_{G.P.}$ (–)
As extruded	5.85×10^{19} (2.6)	20 ± 8	2.45×10^{-4}	/	/	/
Peak-aged T5	5.93×10^{19} (2.6)	18 ± 8	1.81×10^{-4}	0.57×10^{23} (4.9)	3.6 ± 0.8	1.51×10^{-4}
sht	5.6×10^{19} (2.8)	21 ± 9	2.72×10^{-4}	/	/	/
Peak-aged T6	4.91×10^{19} (4.6)	24 ± 9	3.55×10^{-4}	2.63×10^{23} (4.4)	2.8 ± 0.7	4.22×10^{-4}

reconstruction, purple-colored isoconcentration surfaces display gradient concentrations of 2.1 at.% (Al + Ca), marking the G.P. zones. Magnification of one such G.P. zone (inset to Fig. 9a) shows that Al alone is present in an ordered, mono-layered plane, whereas Ca atoms are situated diffusely around it. Because HR-STEM imaging has shown clearly that the G.P. zones appear as ordered monolayers (inset to Fig. 8b), the apparent delocalization of Ca observed in the APT atom map is ascribed to the combined impact of preferential evaporation and local magnification APT artefacts [38,39]. For this reason, isoconcentration-surface analysis was chosen, which includes a volume rather than a mono-layered precipitate, thereby considering both Al and Ca. Proximity histograms extracted from these precipitates reveal an Al-to-Ca ratio of about 2–2.5 within the G.P.-zone volume (Fig. 9b). Preferential presence of Mn at the site of G.P. zones was detected, although their contribution to G.P.-zone formation is minor at about 0.2 at.% within the G.P. zones compared to 0.03 at.% in the matrix. Due to the fine-scale dimensions of the G.P. zones, the local magnification and preferential evaporation artefacts limit a clear statement on the amount of Mg atoms in the G.P. zones.

In addition, Ca-solute clusters are occasionally observed which are locally separated from the G.P. zones. These Ca clusters are depicted in Fig. 9a (arrows) as red-colored isoconcentration surfaces and display a gradient concentration of 0.65 at.% Ca. It was found that they contain only a small amount of Al (Fig. 9c) and are, at about 0.7–1.5 nm in radius, considerably smaller in size than the ordered G.P. zones. Finally, the matrix composition was retrieved from the APT data, and the alloying elements amount to 0.20 at.% Al, 0.09 at.% Ca and 0.03 at.% Mn.

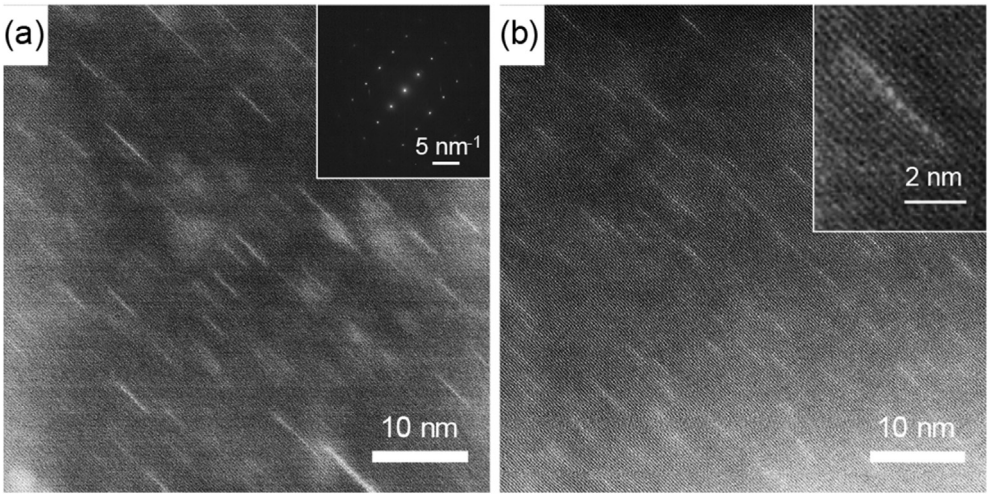

Fig. 8. HAADF images for (a) *peak-aged T5* (taken along the <2$\bar{1}$10] direction) and (b) *peak-aged T6* (taken along the <10$\bar{1}$0] direction). The inset to (a) shows the diffraction pattern of the matrix. The inset to (b) shows the magnification of a single monolayered G.P. zone.

5. Discussion

Here we consider the microstructural contributors to the mechanical properties of AXM100 and distinguish between the material's strength in its *as-extruded* condition, referred to as *base strength*, and that after age hardening. The composition, structure and volume fraction of the two main phases, Al–Mn dispersoids and G.P. zones, are evaluated and compared to the predictions by thermodynamic calculations. In the following estimations, basal slip is assumed to be the only active slip system. This assumption is based on the grain-size regime determined for the alloy studied in which basal slip largely dominates over other slip systems.

5.1. G.P. zones

This study shows that AXM100 in both conditions, *T5* and *T6*, experiences a considerable hardness increase upon artificial aging. The hardening response manifests itself in a significant improvement in *TYS* for both conditions (Fig. 4). The aging response is attributed to ordered mono-layered G.P. zones that form on the basal plane of the hexagonal Mg lattice (Fig. 8). Their roughly 5 times larger number density and 20% smaller size in the *peak-aged T6* compared to the *peak-aged T5* condition (Table 2) account for the larger hardness increment (Fig. 3) and the increase in *TYS* (Fig. 4).

The contribution of precipitation hardening is estimated using equation (1) [40], which allows describing the particle-dislocation interaction for the case of shearable obstacles:

$$\Delta TYS_{\mathrm{G.P.}} = \sqrt{\frac{3}{4\pi\beta}}\,\frac{k_2^3 M\mu}{\sqrt{b}}\,\sqrt{f_{\mathrm{G.P.}}\,\frac{d_{\mathrm{G.P.}}}{2}} \qquad (1)$$

In this equation, β is a parameter equal to 0.5 according to [40], k is a measure for the obstacle strength, M is the Taylor factor with 3 for polycrystalline Mg alloys, μ is the matrix shear modulus with 17 GPa, b is the magnitude of the burgers vector with 3.2 Å, and $f_{\mathrm{G.P.}}$ is the volume fraction of the G.P. zones derived from their number density $N_{\mathrm{G.P.}}$ and volume. The latter is calculated for mono-layered plates with the thickness taken as the Mg interplanar distance of 0.26 nm and the average diameter $d_{\mathrm{G.P.}}$, as given in Table 2. With these values and by adjustment of k to about 0.161, ΔTYS can be fairly well matched with $\Delta TYS^{\mathrm{T5}}_{\mathrm{calc.}} = 66$ MPa and $\Delta TYS^{\mathrm{T6}}_{\mathrm{calc.}} = 98$ MPa to the experimental values of $\Delta TYS^{\mathrm{T5}}_{\mathrm{exp.}} = 71$ MPa and

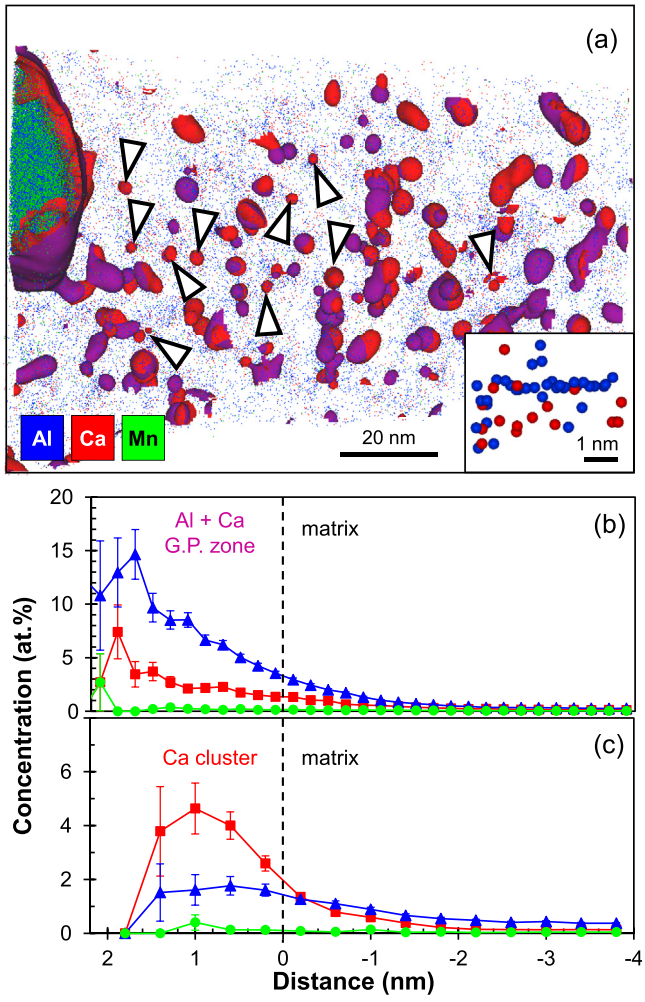

Fig. 9. (a) 3D-reconstruction of *peak-aged T6* temper obtained by APT. The reconstruction includes isoconcentration surfaces for the conditions $c_{\mathrm{Al+Ca}} = 2.1$ at.% and $c_{\mathrm{Ca}} = 0.65$ at.%. Inset: Magnified view of a single G.P. zone. (b–c) Proximity histograms showing the elemental concentrations of Al, Ca and Mn as a function of distance from the precipitate-matrix or cluster-matrix boundary for the isoconcentration surfaces of (b) G.P. zones and (c) Ca clusters. Ca clusters are marked with white arrows in (a). (For interpretation of the references to color in this figure legend, the reader is referred to the Web version of this article.)

$\Delta TYS^{T6}_{exp.} = 97$ MPa, respectively. The close to equal value of k for *T5* and *T6* required to match the experimental values suggests that indeed the same type of hardening mechanism operates in both conditions.

The chemical composition of the G.P. zones was investigated using a correlative approach combining TEM and APT. HR-STEM images reveal an ordered, mono-layered arrangement of heavier atoms in the G.P. zone (inset to Fig. 8b), indicating Ca, which has a significantly higher atomic number than Mg and Al, thus exhibiting a brighter contrast. Conversely, Al has an atomic number close to that of Mg, making its appearance non-distinguishable in an Mg matrix. The limited visibility of Al atoms in STEM imaging can be compensated by APT analysis, which reveals that Al is present as mono-layered precipitates. For Ca, however, APT suffers from an artefact due to a potential preferential field-evaporation rate of Ca compared to Al [38]. Based on the combination of these two methods it can be concluded that G.P. zones are composed of both Al and Ca atoms as previously reported [22,41] and suggested by the thermodynamic calculations (Fig. 1c). Isoconcentration-surface analysis using APT reveals that the Al-to-Ca ratio is about 2–2.5. This ratio differs from the previously reported composition of Mg-Ca6-Al7 (in at.%) [22], obtained for G.P. zones of about 3 nm in size in the Mg–Al–Ca system. The significant contribution of Mg, however, which is reported in Ref. [22] and also observed in the present study, cannot be definitely ascribed to the G.P. zones but may stem from local magnification effects, a known artefact in APT when field-evaporating different phases [39].

The minor contribution of Mn to the G.P. zones detected was previously observed by Homma et al. [41] and explained by the high affinity of Mn to Al, which causes a replacement of Ca by Mn. APT also revealed a size dependence of the G.P.-zone composition. While the majority of G.P. zones (in *T6 peak-aged* condition) appear to have the composition mentioned, with an Al-to-Ca ratio of 2–2.5, smaller precipitates appear to be mainly composed of Ca and present as solute clusters rather than ordered precipitates (Fig. 9).

The size-dependent composition observed is expected to provide an insight into the precipitation sequence of G.P. zones and equilibrium Al_2Ca-phase formation in AXM100: Ca atoms would cluster first, followed by the formation of ordered Al–Ca-rich G.P. zones as metastable precipitates with an Al-to-Ca ratio of about 2–2.5 (Figs. 8 and 9). These are then gradually replaced by the equilibrium Al_2Ca phase [22,24,42], with a predicted C15 structure according to the thermodynamic calculations for AXM100. *sht* not only brings Ca atoms into solid solution, generating an *SSSS* condition, but also leads to a significant fraction of vacancies when the material is water-quenched. These quenched-in vacancies, in combination with the roughly 10-fold greater diffusivity of Ca in Mg compared to Al [43], can explain the initial Ca clustering. This is further supported by the significantly larger solubility of Al in Mg, at about 3.3 at.%, while Ca, which is approximately insoluble at the artificial-aging temperature of 200 °C [25], has a strong tendency to decompose.

Based on these observations, the following precipitation sequence for the Al–Ca phase from *SSSS* for the lean composition AXM100 is proposed:

$$SSSS \rightarrow \begin{matrix}\textit{Ca/solute}\\ \textit{atom}\\ \textit{clusters}\end{matrix} \rightarrow \begin{matrix}\textit{ordered G.P. zones}\\ \textit{with Al:Ca ~2,}\\ \textit{monolayer } (0001)_\alpha\end{matrix} \rightarrow \begin{matrix}\textit{Al}_2\textit{Ca, fcc, C15,}\\ a = 0.802\ \text{nm;}\\ \{111\}_{C15} = (0001)_\alpha\end{matrix}$$

However, in the *as-extruded* state, the Ca atoms required for G.P.-zone formation are not available in solid solution but mainly present in the Mg_2Ca phase, forming Janus particles with the Al–Mn dispersoids (Fig. 7). Note that the co-precipitation of Mg_2Ca at the sites of Al–Mn dispersoids may occur because Ca segregation is facilitated by the strained lattice around the dispersoids. The Mg_2Ca phase is dissolved upon *sht* (Fig. 6b), bringing all Ca in solid solution for an effective hardening response in *T6* condition. In contrast, remnants of Janus particles in the *peak-aged T5* condition (Fig. 6c) show that the Ca reservoir, the Mg_2Ca phase, was not exhausted for the chosen aging parameters of 90 min and 200 °C. Yet the microstructural analysis of the phases reveals a depletion of the Janus particles in *peak-aged T5* compared to the *as-extruded* condition (Fig. 6), providing evidence that the Ca solutes that form the G.P. zones originate from the Mg_2Ca phase. Age hardening can thus still occur despite the capture of Ca in the Mg_2Ca phase in the Janus particles, if one accounts for the high diffusivity of Ca atoms in Mg and the pre-existence of Al atoms in solid solution. Ca is therefore considered to be the main carrier of transformation from the Mg_2Ca equilibrium phase to the metastable Al–Ca phase, present as G.P. zones, at the origin of considerable hardening.

It is to be noted that the solute clusters may present an important contributor to the material strength by impeding dislocation motion, and may account for the difference between the experimentally obtained and expected values. Their role, however, in terms of dislocation interaction, and specifically their obstacle strength, requires a more detailed investigation.

Considering the continuous hardness increase for *T5* condition (Fig. 3), which appears to persist even after 72 h of artificial aging, prolonged aging times may yield a higher hardness increment by achieving complete exhaustion of the Ca reservoir. However, it is not expected that the hardness of *T5* can reach that of *T6* independently of the aging time. This is because the G.P. zones in the *T5* condition precipitate in larger sizes (Table 2), which limits their number density, and is thus detrimental to hardening.

The observation of an incompletely exhausted Ca reservoir in *T5* may also explain the fact that the age-hardening response shows a dependence on extrusion speed only for *T5* but not for *T6* temper, with a faster extrusion resulting in a higher hardness increment for the former (Fig. 3). The friction-induced temperature rise during extrusion, which is higher the faster the extrusion [11], brings the material temperature closer to the solvus temperature of the Mg_2Ca phase, thereby bringing more Ca atoms into solid solution (Fig. 1). This is further supported if the quenching rate after extrusion is considered. This is enhanced when the extrusion speed is faster, because less time passes between the exit of the hot bar and its introduction into the air-quenching system. A fast quenching rate, in turn, prevents the precipitation of Janus particles upon cooling and leaves Ca in solid solution. G.P. zones, which form from *SSSS*, then precipitate in smaller sizes and concurrently in greater number density. This was confirmed by the detailed microstructural analysis of the *peak-aged T6* and its comparison with the *T5* condition. The hardness increment is therefore larger, the more Ca is present in solid solution at the beginning of the artificial-aging treatment. Because for the *T6* condition an *sht* treatment precedes the aging treatment, effectively bringing all Ca atoms into solid solution, no difference in aging response between the two extrusion rates was observed for *T6*.

5.2. Al–Mn dispersoids

Al–Mn dispersoids are prominent microstructural features of the AXM100 material. Because their number density and size are about the same for all four thermomechanical conditions studied, their contribution to age hardening can be excluded. This is, instead, ascribed entirely to the precipitation of the G.P. zones and potentially to the Ca-rich clusters described above. The Al–Mn

dispersoids may, however, play a role in defining the base strength of the material, i.e. that in the non-aged state. In fact, solid-solution strengthening and work hardening can both be disregarded, the former due to the leanness of the alloy and the latter due to a dislocation density which is low enough to be neglected. Only the difference of *TYS* and H_V measured between the *as-extruded* and *sht* condition of about $\Delta TYS = 9$ MPa (Table 1) and $\Delta H_V = 4$ (Fig. 3), respectively, can be ascribed to the dislocation density, which is presumably higher after extrusion but reduced by the high-temperature *sht*. The increment, however, is relatively small. Thus, we can conclude that the base strength of AXM100 is governed by the material's grain size and by precipitation hardening via the Al–Mn dispersoids, present in all conditions (Fig. 6).

The precipitation-hardening contribution of the Al–Mn dispersoids is estimated using the line-tension model [44], which allows to describe the particle-dislocation interaction for the case of dislocation bowing at the obstacle as:

$$\Delta TYS_{\mathrm{Al-Mn}} = \frac{\alpha\, \mu\, b}{l} \tag{2}$$

where α is the obstacle strength. Here it is taken as 1, corresponding to unshearable obstacles, to estimate the greatest possible hardening contribution of the dispersoids. Further, μ is the matrix shear modulus with 17 GPa for Mg, b is the magnitude of the burgers vector with 3.2 Å and l is the interparticle spacing on the glide plane. The latter is derived from the number density $N_{\mathrm{Al-Mn}}$ and size $d_{\mathrm{Al-Mn}}$ of the dispersoids (Table 2) according to the following equation (3) [45], which is expressed as the volume fraction $f_{\mathrm{Al-Mn}}$ and assuming spherical particles:

$$l = \frac{d_{\mathrm{Al-Mn}}}{2\sqrt{f_{\mathrm{Al-Mn}}}} \approx \frac{1}{\sqrt{2\, N_{\mathrm{Al-Mn}}\, d_{\mathrm{Al-Mn}}}} \tag{3}$$

In this approximation only the dispersoids' size and number density are taken into consideration, whereas the dispersoid shape and orientation relative to the matrix, both known to affect the resulting strength [46], are summarized by the parameter α in equation (2). With the values $N_{\mathrm{Al-Mn}}$ and $d_{\mathrm{Al-Mn}}$ from Table 2, the derived strength contribution is at a maximum about 8 MPa. This simplified estimation shows clearly that the Al–Mn dispersoids only play a subordinate role for the material's strength in terms of precipitation hardening. Nevertheless, these thermally stable Al–Mn dispersoids are essential for the material's performance because they present obstacles to grain-boundary movement, as discussed below.

A closer look at the dispersoid's composition, obtained by STEM-EDS measurements (Fig. 7) and confirmed by APT (Fig. 9), indicate that their Mn content exceeds that of Al, as previously observed [29]. This finding is surprising considering the Al_8Mn_5 phase predicted by thermodynamic calculations using the Pandat database and by literature [20,30].

In order to identify the structure of the Al–Mn dispersoids, a detailed analysis was conducted using nanodiffraction. Fig. 10 presents experimental diffraction patterns obtained along two different zone axes in an Al–Mn dispersoid of about 50 nm in size. The periodic spot patterns indicate single-crystallinity, in contrast to a nano-structured precipitate that would yield diffraction with a ring pattern or an aperiodic spot pattern. Each diffraction pattern was tentatively matched with simulated patterns of different candidate structures. The experimentally obtained diffraction patterns (Fig. 10) were carefully analyzed by matching them with simulated ones of different structures from literature, using diffractGUI software. The candidate structures considered were the Al_8Mn_5 phase, as predicted by the thermodynamic simulation (Fig. 1c), in a rhombohedral form [47] and cubic form [48], but also tetragonal $Al_{0.89}Mn_{1.11}$ [49], hexagonal $Al_{0.9}Mn_{1.1}$ [50], cubic AlMn (45:55) [51], cubic β-Mn [52], and α-Mn [53]. The latter two accommodate up to 40 at.% Al, satisfying the condition of Mn being the dominant element. It appears that the best matches between the experimental and simulated patterns were obtained for three structures, namely β-Mn, rhombohedral Al_8Mn_5, and α-Mn. Fig. 10 presents, in addition to two experimental diffraction patterns named 'zone axis 1' and 'zone axis 2', the best matches found for those structures and the corresponding zone axes. Note that they include double diffraction and the first-order Laue zone (FOLZ), in addition to the zero-order Laue zone [54]. It appears that all three structures provide a reasonable fit for zone axis 1, while β-Mn provides the best match for zone axis 2, followed by Al_8Mn_5. In the latter orientation, α-Mn lacks the FOLZ information observed in the outskirts of the experimental pattern and can therefore be excluded. In contrast, in zone axis 1 there are two small FOLZ diffraction spots at the top left of the picture which match with β-Mn only. Further evidence is taken from the angle between the two zone axes. The theoretical angle between the two matching zone axes of β-Mn ([101] and [313]) was 13.26°, and matches rather well with the experimentally applied tilt of 11.5°. In comparison, the theoretical angle between the zone axes of Al_8Mn_5 ([212] and [313]) amounts to 9.4°. From the correlatively analyzed diffraction patterns, the tilt angle, and chemical information obtained from EDS and APT, we can conclude that the Al–Mn dispersoids are of β-Mn type. This finding is associated with the recently reported co-existence of Al_8Mn_5 and β-Mn phase in an AXM10203 alloy [20]; however, no Al_8Mn_5 precipitates were identified in this study.

5.3. Mg_2Ca phase

Evaluating the contribution of the phases present to precipitation hardening, the role of the Mg_2Ca phase as part of the Janus particles is, likewise, a minor one. We come to this conclusion by considering their size which is similar to that of the Al–Mn dispersoids and, more importantly, their co-presence with the Al–Mn dispersoids (Fig. 7). The nature of Janus particles approximately doubles the overall obstacle size, which, however, only negligibly reduces the significantly larger interparticle spacing on the slip plane. Because the latter is by far the stronger determining factor in precipitation hardening according to Eq. (2), the Mg_2Ca phase cannot strengthen the material considerably. In sum, the strength contribution of both Al–Mn dispersoids and Mg_2Ca phase are minor in comparison with the experimentally obtained base hardness and base strength in the *as-extruded* state.

5.4. Grain size

Finally, the grain size as a contributor to the material's base strength is assessed. Its contribution is estimated by the well-known *Hall–Petch* equation [3,4]:

$$\Delta TYS_{\text{grain size}} = \; k_y\, D^{-1/2} \tag{4}$$

where k_y is the *Hall–Petch* coefficient at 150–250 MPa $\mu m^{1/2}$ [5,6] and D is the average grain size. With D at about 30 μm, the contribution of grain-boundary strengthening to *TYS* amounts to a maximum of about 45 MPa. Note that with these values there is a discrepancy between the estimated and experimental base-strength value ($TYS^{sht} = 156$ MPa). The former is at most at about 70 MPa as derived from summing the friction stress for dislocation movement, reported to be 12–18 MPa for Mg [5,55], the dispersoid's maximum strength contribution of about 8 MPa, and the grain-boundary strengthening of 45 MPa. In this estimation,

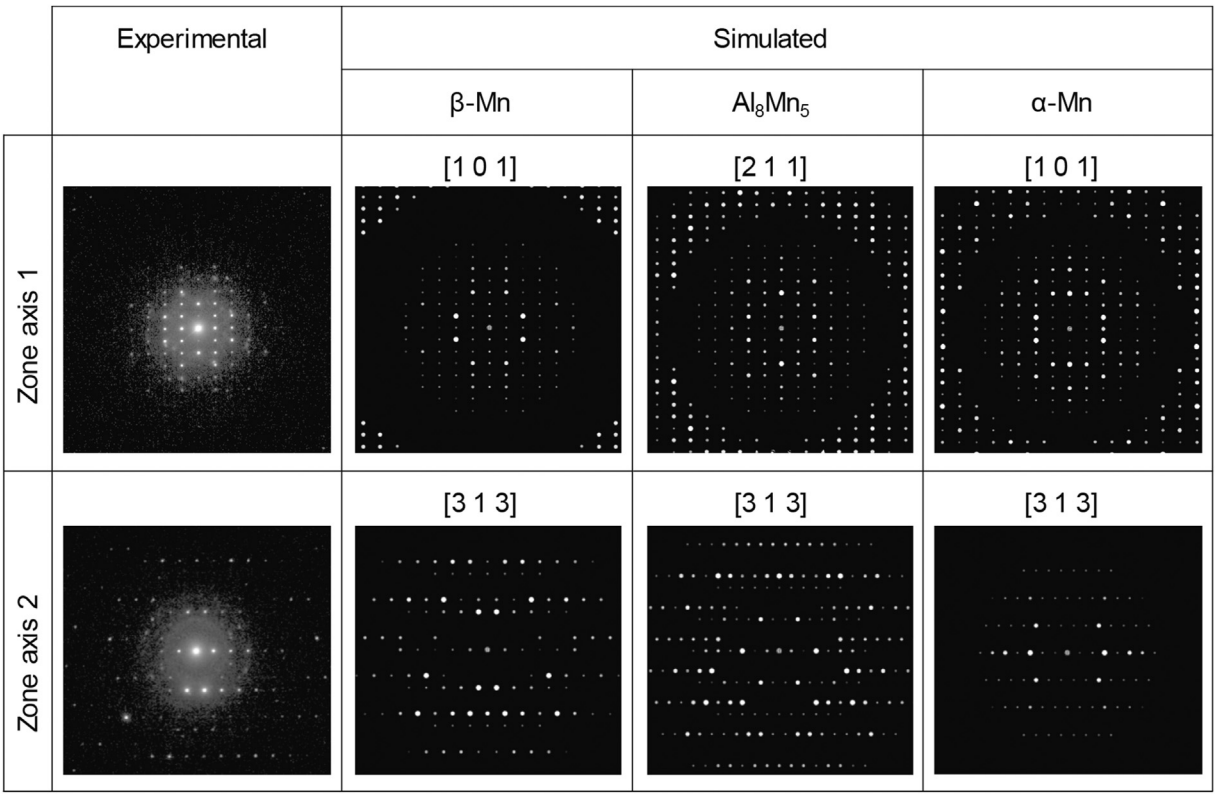

Fig. 10. Left: Spot patterns experimentally obtained by nanodiffraction in two different zone axes of the Al–Mn dispersoids. Right: Simulated patterns for three reported possible structures, β-Mn, Al_8Mn_5 and α-Mn.

however, we have not considered the contribution of solid-solution hardening of Al and Ca and texture effects. Nevertheless, from these simple calculations at the given boundary conditions, it can be concluded that the grain size significantly dominates the *TYS* over the Al–Mn dispersoids.

The essence of the Al–Mn dispersoids, however, comes into play as obstacles for grain-boundary motion, thereby impeding grain growth at elevated temperatures. Indeed, the material resists excessive grain coarsening; this is experimentally evident from the approximately constant average grain size in all four thermo-mechanical conditions studied, with only a minor increase upon *sht*, and was previously observed in the AXM system [20,29]. The obstacle-mediated grain-growth limitation, referred to as *Zener* drag, provides a maximum grain size D_{max}, which can be estimated by the *Zener–Smith* equation [13]:

$$D_{max} = \frac{2\, d_{Al-Mn}}{3\, f_{Al-Mn}} \tag{5}$$

where d and f are the dispersoid diameter and volume fraction, respectively. From this equation the maximum grain size amounts to about 60 μm. This agrees fairly well with the experimentally determined average grain size of about 30 μm, noting the presence of a few coarse and significantly larger grains, especially in the center of the extruded bar (Fig. 5).

In light of the essential contribution of grain-boundary strengthening, the resistance to grain coarsening upon *sht* is crucial to maintaining the benefits of a substantial age-hardening response in the *T6* temper. It is therefore an essential aspect of the performance of AXM100 as a hardenable lean wrought-alloy.

The grain size is not only crucial for the material's strength, but can also explain the low ductility observed (Table 1). In Mg alloys different grain-size levels result in different deformation modes to be active [56,57]. This is, *inter alia*, expressed in a raised probability of twin deformation over slip deformation at increased grain size [57,58]. The presence of twins may be the cause of the low elongation to fracture observed (Fig. 4), because in Mg alloys twin boundaries can act as crack nucleation sites [11,59]. In fact, twin formation was frequently observed in this AXM100 alloy and in related representatives of this alloy system, independently of the thermomechanical condition (data not shown). In this light, the occasionally observed significantly larger grains (> 60 μm) (Fig. 5) are detrimental and a reduction of the grain size to below the critical value at which slip deformation dominates over twinning deformation would thus improve ductility [57,60]. This appears feasible by modification of the extrusion-process parameters towards a reduced extrusion temperature [61]. A lower extrusion temperature would simultaneously allow an increase of the extrusion speed (Fig. 2), provided that an extrusion device without the present force limitation was used.

The critical grain size, at which non-basal slip occurs over twin deformation, was observed by Kobayashi et al. as 7 μm [62] for AZ31. This was later supported by Wang et al. [60] to be 4 μm. The reduction in grain size would thus lead, apart from an expected improvement in ductility, to an enhanced *TYS*. An estimate of *TYS* based on Eq. (4), with a grain size of 4 μm and with the same *Hall–Petch* constant as above ($k_y = 250$ MPa $\mu m^{1/2}$), yields 125 MPa, which is about 175% higher than the *TYS* obtained for a grain size of 30 μm.

It should, however, be mentioned that with a reduction in grain size to a range where non-basal slip systems are activated, the hardening effectiveness of the G.P. zones is expected to decline. This is because G.P. zones precipitating on the basal plane (Fig. 8) would become less effective as obstacles to slip, when increasing the likelihood of non-basal slip with a reduction in grain size. The

Table 3
Comparison of AXM-alloys as to their age-hardening potential in light of the lean-alloying concept.

Alloy	Composition in wt.% (at.%)	Condition	*TYS* in peak-aged condition (MPa)	Δ*TYS* (MPa)	Δ*TYS*/(Al + Ca + Mn) (MPa/at.%)	Reference
AXM100	Al0.6(0.54)-Ca0.28(0.17)-Mn0.25(0.11)	T5	236	71	87	This study
AXM0301502	Al0.30(0.27)-Ca0.21(0.13)-Mn0.47(0.21)	T5	207	37	61	[32]
AXM030204	Al0.27(0.30)-Ca0.31(0.19)-Mn0.84(0.37)	T5	210	20	23	[33]
AXM030304	Al0.34(0.32)-Ca0.32(0.19)-Mn0.43(0.19)	T5	220	54	77	[29]
AXM030302	Al0.33(0.30)-Ca0.34(0.20)-Mn0.24(0.11)	T5	188	52	85	[29]
AXM100	Al0.6(0.54)-Ca0.28(0.17)-Mn0.25(0.11)	T6	253	97	118	This study
AXM1021	Al1.08(0.98)-Ca0.24(0.15)-Mn1.03(0.46)	T6	263	68	43	[20, 63]
AXM10304	Al1.31(1.19)-Ca0.33(0.20)-Mn0.46(0.21)	T6	287	100	63	[17]

reported threshold value below which non-basal slip systems are activated, and enable dislocations to bypass the G.P. zones, is about 4–7 μm. The optimal grain size is thus to be balanced in order to benefit from both mechanisms, namely grain refinement and precipitation strengthening.

5.5. Comparison of experimental data and calculations

The insights gained into the various precipitation phases, in terms of their phase composition and volume fraction, are now compared with the values predicted by the thermodynamic calculations. The calculations had predicted Al_8Mn_5 and Al_2Ca as the phases presenting the dispersoids blocking the grain boundaries and the precipitates composing the hardening phase, respectively. Fig. 1 presents their calculated volume fractions. The content of alloying elements and their ratios were balanced accordingly. Microstructural analysis of the resulting alloy revealed, however, that the predicted Al_8Mn_5 phase is indeed a β-Mn phase, which accommodates up to 40 at.% Al (Figs. 7d and 9). The calculations therefore overestimated the Al content required to form the Al–Mn phase. In contrast, they supported the suggested Al-to-Ca ratio of 2 for the formation of G.P. zones. While due to local magnification effects in APT analysis no conclusive statement can be made as to the contribution of Mg to the G.P. zones, its contribution would likewise lead to an overestimation of the Al content. Recalculation, taking into account the lower demand in Al, may therefore produce an improved alloy composition.

The phase volume fractions were estimated for the *peak-aged T6* condition using the experimentally obtained sizes and number densities (Table 2). This estimation shows a significantly lower volume fraction for both phases, with 3.6×10^{-4} and 4.2×10^{-4} for the Al–Mn and the Al–Ca phase, respectively, than predicted by thermodynamic simulations, with 2.3×10^{-3} and 5.0×10^{-3}, respectively. Keeping in mind that the calculation assumes thermodynamic equilibrium, this result is not surprising and suggests that equilibrium is not reached in *peak-aged T6* condition. This is supported by the matrix composition derived from APT analysis, which with 0.2 at.% Al, 0.09 at.% Ca and 0.03 at.% Mn accommodates a significantly larger solute content than that predicted by the calculations: 0.09 at.% Al, 0.001 at.% Ca and 1.5×10^{-6} at.% Mn. Taking this higher remaining matrix's solute content and the overestimated Al need for the Al–Mn-dispersoid formation into account, it is suggested that the Al content could be reduced further without negatively affecting the hardening potential. This would benefit an even leaner alloy composition.

The design concept envisages an *sht* window for obtaining complete solution of Ca. Indeed, the microstructural analysis shows that the Mg_2Ca phase, present in the Janus particles in the *as-extruded* condition (Fig. 6a), is completely dissolved upon exposure to 510 °C for 10 min (Fig. 6b). The solvus temperature of the Mg_2Ca phase is predicted to be at about 460 °C (Fig. 1c). On this basis an extrusion temperature of 450 °C was chosen, which, considering the friction-induced temperature raise, gains a high Ca content in solution in the *as-extruded* condition. The presence of a significant volume fraction of Mg_2Ca phase in the *as-extruded* state (Fig. 6a) suggests, however, that either the real solvus temperature of the Mg_2Ca phase is higher than the predicted value, or that this phase precipitates during cooling from the extrusion temperature.

Table 3 compares the alloy developed in this study with other AXM alloys reported in literature. The alloys' *TYS* in the peak-aged condition for both *T5* and *T6* are compared as well as their hardening increment upon artificial aging (Δ*TYS*). In addition, the latter is normalized by the total alloying-element content, giving a value Δ*TYS* per at.% total alloying-element content. This normalized value is used to evaluate the alloy's age-hardening potential in light of the envisaged lean-alloy concept. In fact, for both *T5* and *T6* the normalized hardening increment is at 87 MPa/at.% for *T5* condition and 118 MPa/at.% for *T6* condition the largest among those of the alloys reported. The alloy which shows the most attractive mechanical properties thus far is AXM10304, developed by Nakata et al. [17]. This alloy shows a remarkable combination of high *TYS* and Δ*TYS*: 287 MPa and 100 MPa, respectively. Due to the low processing temperature of 275 °C, however, a *T6* treatment is implied in order to bring enough Ca in solution. This excludes the economically more attractive *T5* processing route. The AXM100, in contrast, processed here at 450 °C, has the drawback of a coarsened grain size. However, it shows significant hardening also in *T5*, making it an attractive candidate for industrial applications.

Assuming that the attainable extrusion speed depends on the amount of solute atoms and secondary-phase particles in the matrix, our alloy, with less than 1 at.% of alloying elements, may be an ideal candidate for high-speed extrusion, provided that a suitable extrusion machine with a greater possible extrusion force is deployed. If extrapolated to 275 °C from the green triangle in Fig. 2, an extrusion speed of roughly 20 m min^{-1} could be achieved. This value accords with the regime reported in Ref. [17].

6. Conclusions

In this study we have rationally designed a lean AXM alloy using thermodynamic calculations comprising its composition and the thermomechanical treatment conditions for its production. The strength of the developed alloy, Mg-Al0.6-Ca0.28-Mn0.25, in wt.%, was evaluated by tensile testing, with a particular focus on its potential for hardening upon artificial aging. The mechanical properties were studied in conjunction with an assessment of the microstructure using TEM and APT to understand the origin of the material's strength at the nanometric scale. The main conclusions drawn are as follows:

- Despite the very low alloying content of less than 1 at.%, our AXM100 alloy exhibits substantial hardening upon artificial aging at 200 °C for 90 min: Δ*TYS* ≈ 70 MPa for *T5* condition and

100 MPa for *T6* condition, reaching a *TYS* of 253 MPa for the latter.

- Scattered Al–Mn dispersoids of about 20 nm in size are present in all conditions, indicating their thermal stability. They successfully retard grain growth during *sht*.
- Nanodiffraction combined with STEM-EDS and APT analysis reveals that the Al–Mn dispersoids are composed of β-Mn phase, with a composition close to $Mn_{60}Al_{40}$ (in at.%).
- Further grain refinement would increase the alloy's strength, and help increase the material's ductility by activating non-basal dislocation slip.
- Ordered G.P. zones precipitating densely on the basal plane of the Mg matrix are responsible for the significant hardening response upon artificial aging. Their nanometric size is smaller and their number density larger in the *T6* condition than in the *T5* condition, explaining the larger hardening increment in *T6*.
- Correlative analysis combining high-resolution STEM and APT allows us to infer that the G.P. zones are thin plates composed of Al and Ca with a ratio of about 2, which is close to the equilibrium phase composition Al_2Ca.
- Ca plays a key role in the precipitation of the Al–Ca G.P. zones from solid solution (*T6* condition) and originates from the dissolution of the Mg_2Ca phase (*T5* condition). This is facilitated by its insolubility at low temperature and its high diffusivity in Mg.
- The Mg_2Ca phase co-precipitates at the sites of the Al–Mn dispersoids, forming Janus particles in the *as-extruded* state. The Mg_2Ca phase serves as a Ca reservoir for the formation of Al–Ca-rich G.P. zones.
- Nanometric Ca-rich clusters were identified by APT that may not only act as precursors to G.P. zones, but also contribute to the alloy's strength.
- Thermodynamic calculations, provided the limitations assessed in this work are taken into account, prove to be an invaluable tool for the rational design of hardenable Mg-based lean alloys.

Acknowledgements

The authors acknowledge D. Horwatitsch, T. Hametner, S. Gneiger and C. Schlögl from LKR Leichtmetallkompetenzzentrum Ranshofen GmbH Austria for providing the material. Technical support by Christian Wegmann (LMPT, ETH Zurich) and experimental support by Giulia Biffi (LMPT, ETH Zurich) in determining the mechanical properties are gratefully acknowledged. The authors appreciate the support of the Austrian Research Promotion Agency (FFG Grant No. 843537), the Swiss National Science Foundation (SNF Grant No. 200021-157058), and the Scientific Center for Optical and Electron Microscopy (ScopeM), ETH Zurich.

References

[1] C. Davies, M. Barnett, Expanding the extrusion limits of wrought magnesium alloys, JOM Journal of the Minerals, Metals Mater. Soc. 56 (5) (2004) 22–24.
[2] D.L. Atwell, M.R. Barnett, Extrusion limits of magnesium alloys, Metall. Mater. Trans. A 38 (12) (2007) 3032–3041.
[3] E. Hall, The deformation and ageing of mild steel: III discussion of results, Proc. Phys. Soc.. Sec. B 64 (9) (1951) 747.
[4] N.J. Petch, The cleavage strengh of polycrystals, J. Iron and Steel Inst. 174 (1953) 25–28.
[5] P. Andersson, C.H. Cáceres, J. Koike, Hall-Petch parameters for tension and compression in cast Mg, Mater. Sci. Forum, Trans. Tech. Publ. (2003) 123–128.
[6] D. Wilson, J. Chapman, Effects of preferred orientation on the grain size dependence of yield strength in metals, Phil. Mag. 8 (93) (1963) 1543–1551.
[7] N. Hansen, The effect of grain size and strain on the tensile flow stress of aluminium at room temperature, Acta Metall. 25 (8) (1977) 863–869.
[8] A. Yamashita, Z. Horita, T.G. Langdon, Improving the mechanical properties of magnesium and a magnesium alloy through severe plastic deformation, Mater. Sci. Eng. 300 (1–2) (2001) 142–147.
[9] M. Kai, Z. Horita, T.G. Langdon, Developing grain refinement and superplasticity in a magnesium alloy processed by high-pressure torsion, Mater. Sci. Eng. 488 (1–2) (2008) 117–124.
[10] M. Mabuchi, T. Asahina, H. Iwasaki, K. Higashi, Experimental investigation of superplastic behaviour in magnesium alloys, Mater. Sci. Technol. 13 (10) (1997) 825–831.
[11] M. Jiang, C. Xu, T. Nakata, H. Yan, R. Chen, S. Kamado, High-speed extrusion of dilute Mg-Zn-Ca-Mn alloys and its effect on microstructure, texture and mechanical properties, Mater. Sci. Eng. 678 (2016) 329–338.
[12] J. Hofstetter, S. Rüedi, I. Baumgartner, H. Kilian, B. Mingler, E. Povoden-Karadeniz, S. Pogatscher, P.J. Uggowitzer, J.F. Löffler, Processing and microstructure–property relations of high-strength low-alloy (HSLA) Mg–Zn–Ca alloys, Acta Mater. 98 (2015) 423–432.
[13] C. Zener, Quoted by CS Smith, Trans. AIME 175 (1948) 15.
[14] J.-F. Nie, Precipitation and hardening in magnesium alloys, Metall. Mater. Trans. A 43 (11) (2012) 3891–3939.
[15] K. Oh-Ishi, R. Watanabe, C. Mendis, K. Hono, Age-hardening response of Mg–0.3 at.% Ca alloys with different Zn contents, Mater. Sci. Eng. 526 (1) (2009) 177–184.
[16] S. Celotto, TEM study of continuous precipitation in Mg–9 wt% Al–1 wt% Zn alloy, Acta Mater. 48 (8) (2000) 1775–1787.
[17] T. Nakata, C. Xu, R. Ajima, K. Shimizu, S. Hanaki, T. Sasaki, L. Ma, K. Hono, S. Kamado, Strong and ductile age-hardening Mg-Al-Ca-Mn alloy that can be extruded as fast as aluminum alloys, Acta Mater. 130 (2017) 261–270.
[18] Z. Li, X. Zhang, M. Zheng, X. Qiao, K. Wu, C. Xu, S. Kamado, Effect of Ca/Al ratio on microstructure and mechanical properties of Mg-Al-Ca-Mn alloys, Mater. Sci. Eng. 682 (2017) 423–432.
[19] S. Xu, K. Oh-Ishi, S. Kamado, F. Uchida, T. Homma, K. Hono, High-strength extruded Mg–Al–Ca–Mn alloy, Scripta Mater. 65 (3) (2011) 269–272.
[20] T. Nakata, C. Xu, R. Ajima, Y. Matsumoto, K. Shimizu, T. Sasaki, K. Hono, S. Kamado, Improving mechanical properties and yield asymmetry in high-speed extrudable Mg-1.1 Al-0.24 Ca (wt.%) alloy by high Mn addition, Mater. Sci. Eng. 712 (2018) 12–19.
[21] N. Stanford, The effect of calcium on the texture, microstructure and mechanical properties of extruded Mg–Mn–Ca alloys, Mater. Sci. Eng. 528 (1) (2010) 314–322.
[22] J. Jayaraj, C. Mendis, T. Ohkubo, K. Oh-Ishi, K. Hono, Enhanced precipitation hardening of Mg–Ca alloy by Al addition, Scripta Mater. 63 (8) (2010) 831–834.
[23] J.B. Clark, Age hardening in a Mg-9 wt.% Al alloy, Acta Metall. 16 (2) (1968) 141–152.
[24] A. Suzuki, N. Saddock, J. TerBush, B. Powell, J. Jones, T. Pollock, Precipitation strengthening of a Mg-Al-Ca–based AXJ530 die-cast alloy, Metall. Mater. Trans. A 39 (3) (2008) 696–702.
[25] A. Nayeb-Hashemi, J.B. Clark, Phase Diagrams of Binary Magnesium Alloys, ASM International, Metals Park, 1988. Ohio 44073, USA.
[26] J. She, F. Pan, W. Guo, A. Tang, Z. Gao, S. Luo, K. Song, Z. Yu, M. Rashad, Effect of high Mn content on development of ultra-fine grain extruded magnesium alloy, Mater. Des. 90 (2016) 7–12.
[27] L. Tong, M. Zheng, S. Xu, S. Kamado, Y. Du, X. Hu, K. Wu, W. Gan, H. Brokmeier, G. Wang, Effect of Mn addition on microstructure, texture and mechanical properties of Mg–Zn–Ca alloy, Mater. Sci. Eng. 528 (10) (2011) 3741–3747.
[28] S.A. Khan, Y. Miyashita, Y. Mutoh, Z.B. Sajuri, Influence of Mn content on mechanical properties and fatigue behavior of extruded Mg alloys, Mater. Sci. Eng. 420 (1) (2006) 315–321.
[29] T. Nakata, C. Xu, Y. Matsumoto, K. Shimizu, T. Sasaki, K. Hono, S. Kamado, Optimization of Mn content for high strengths in high-speed extruded Mg-0.3 Al-0.3 Ca (wt%) dilute alloy, Mater. Sci. Eng.: A 673 (2016) 443–449.
[30] L. Han, H. Hu, D.O. Northwood, N. Li, Microstructure and nano-scale mechanical behavior of Mg–Al and Mg–Al–Ca alloys, Mater. Sci. Eng. 473 (1–2) (2008) 16–27.
[31] CompuTherm LLC, Pandat Software Package for Calculating Phase Diagrams and Thermodynamic Properties of Multi- Component Alloys, Madison, USA, www.computherm.com.
[32] T. Nakata, T. Mezaki, R. Ajima, C. Xu, K. Oh-Ishi, K. Shimizu, S. Hanaki, T. Sasaki, K. Hono, S. Kamado, High-speed extrusion of heat-treatable Mg–Al–Ca–Mn dilute alloy, Scripta Mater. 101 (2015) 28–31.
[33] T. Nakata, K. Shimizu, Y. Matsumoto, S. Hanaki, S. Kamado, Effect of Mn Content on Microstructures and Mechanical Properties of Mg-al-ca-mn Alloys Fabricated by High-speed Extrusion, Magnesium Technology 2015, Springer, 2015, pp. 241–246.
[34] I.O.f.S. (ISO), Aluminium and Aluminium Alloys, Wrought Products - Temper Designations, 2007.
[35] M. Klinger, A. Jäger, Crystallographic Tool Box (CrysTBox): automated tools for transmission electron microscopists and crystallographers, J. Appl. Crystallogr. 48 (6) (2015) 2012–2018.
[36] P. Stadelmann, EMS-a software package for electron diffraction analysis and HREM image simulation in materials science, Ultramicroscopy 21 (2) (1987) 131–145.
[37] P.K. Saha, Aluminum extrusion technology, ASM Int., 2000, ISBN 0-87170-644-X.
[38] M. Miller, G. Smith, An atom probe study of the anomalous field evaporation of alloys containing silicon, J. Vac. Sci. Technol. 19 (1) (1981) 57–62.
[39] M. Miller, M. Hetherington, Local magnification effects in the atom probe, Surf. Sci. Lett. 246 (1–3) (1990) A181.
[40] A. Deschamps, Y. Brechet, Influence of predeformation and ageing of an

Al–Zn–Mg alloy—II. Modeling of precipitation kinetics and yield stress, Acta Mater. 47 (1) (1998) 293–305.
[41] T. Homma, S. Nakawaki, K. Oh-Ishi, K. Hono, S. Kamado, Unexpected influence of Mn addition on the creep properties of a cast Mg–2Al–2Ca (mass%) alloy, Acta Mater. 59 (20) (2011) 7662–7672.
[42] T. Homma, S. Hirawatari, H. Sunohara, S. Kamado, Room and elevated temperature mechanical properties in the as-extruded Mg–Al–Ca–Mn alloys, Mater. Sci. Eng. 539 (2012) 163–169.
[43] B.-C. Zhou, S.-L. Shang, Y. Wang, Z.-K. Liu, Diffusion coefficients of alloying elements in dilute Mg alloys: a comprehensive first-principles study, Acta Mater. 103 (2016) 573–586.
[44] D. Hull, D.J. Bacon, Introduction to Dislocations, vol. 37, Elsevier, 2011, ISBN 008096673X.
[45] J.W. Martin, Micromechanisms in Particle-hardened Alloys, CUP Archive, 1980, ISBN 0521295807.
[46] J. Nie, Effects of precipitate shape and orientation on dispersion strengthening in magnesium alloys, Scripta Mater. 48 (8) (2003) 1009–1015.
[47] J. Visser, On the structure of (Cr5Al8) 26R. A correction, Acta Crystallogr. Sect. B Struct. Crystallogr. Cryst. Chem. 33 (1) (1977) 316.
[48] J. Braun, M. Ellner, B. Predel, Structure of the high-temperature phase Cr5al8(H), J. Alloy. Comp. 183 (1992) 444–448.
[49] P.B. Braun, J.A. Goedkoop, An X-ray and neutron diffraction investigation of the magnetic phase Al0. 89Mn1. 11, Acta Crystallogr. 16 (8) (1963) 737–740.
[50] W. Koster, E. Wachtel, Aufbau und magnetische eigenschaften der aluminium-mangan-legierungen mit mehr als 25-at-Percent Mn, Z. Fur Metallkunde 51 (5) (1960) 271–280.
[51] M. Ellner, The structure of the high-temperature phase MnAl (h) and the displacive transformation from MnAl (h) into Mn5Al8, Metall. Trans. A 21 (6) (1990) 1669–1672.
[52] C.B. Shoemaker, D.P. Shoemaker, T. Hopkins, S. Yindepit, Refinement of the structure of β-manganese and of a related phase in the Mn–Ni–Si system, Acta Crystallogr. Sect. B Struct. Crystallogr. Cryst. Chem. 34 (12) (1978) 3573–3576.
[53] A. Bradley, J. Thewlis, The crystal structure of α-manganese, in: Proceedings of the Royal Society of London. Series A, containing Papers of a Mathematical and Physical Character, 115, 1927, pp. 456–471, 771.
[54] D.B. Williams, C.B. Carter, Transmission Electron Microscopy - a Textbook for Materials Science, Plenum Press, 1996, ISBN 030645324X.
[55] C. Caceres, G.E. Mann, J. Griffiths, Grain size hardening in Mg and Mg-Zn solid solutions, Metall. Mater. Trans. A 42 (7) (2011) 1950–1959.
[56] J. Koike, T. Kobayashi, T. Mukai, H. Watanabe, M. Suzuki, K. Maruyama, K. Higashi, The activity of non-basal slip systems and dynamic recovery at room temperature in fine-grained AZ31B magnesium alloys, Acta Mater. 51 (7) (2003) 2055–2065.
[57] M. Barnett, Z. Keshavarz, A. Beer, D. Atwell, Influence of grain size on the compressive deformation of wrought Mg–3Al–1Zn, Acta Mater. 52 (17) (2004) 5093–5103.
[58] S. Xu, K. Oh-ishi, H. Sunohara, S. Kamado, Extruded Mg–Zn–Ca–Mn alloys with low yield anisotropy, Mater. Sci. Eng. 558 (2012) 356–365.
[59] F. Yang, S. Yin, S. Li, Z. Zhang, Crack initiation mechanism of extruded AZ31 magnesium alloy in the very high cycle fatigue regime, Mater. Sci. Eng. 491 (1–2) (2008) 131–136.
[60] J.T. Wang, J.Q. Liu, J. Tao, Y.L. Su, X. Zhao, Effect of grain size on mechanical property of Mg–3Al–1Zn alloy, Scripta Mater. 59 (1) (2008) 63–66.
[61] T. Nakata, T. Mezaki, C. Xu, K. Oh-ishi, K. Shimizu, S. Hanaki, S. Kamado, Improving tensile properties of dilute Mg-0.27 Al-0.13 Ca-0.21 Mn (at.%) alloy by low temperature high speed extrusion, J. Alloy. Comp. 648 (2015) 428–437.
[62] T. Kobayashi, J. Koike, Y. Yoshida, S. Kamado, M. Suzuki, K. Maruyama, Y. Kojima, Grain size dependence of active slip systems in an AZ 31 magnesium alloy, J. Jpn. Inst. Metals 67 (4) (2003) 149–152.
[63] T. Nakata, C. Xu, T. Sasaki, Y. Matsumoto, K. Shimizu, K. Hono, S. Kamado, Development of high-strength high-speed-extrudable Mg–Al–Ca–Mn alloy, Magnesium Technol. (2017) 17–21. Springer2017.